H I KINEMATICS AND DYNAMICS OF MESSIER 31[*]

LAURENT CHEMIN[1], CLAUDE CARIGNAN[2,3], AND TYLER FOSTER[4]
[1] GÉPI, Observatoire de Paris, Section Meudon & Université Paris 7, 5 Place Jules Janssen, 92195 Meudon, France; Laurent.Chemin@obspm.fr
[2] Laboratoire d'Astrophysique Expérimentale (LAE), Observatoire du mont Mégantic, and Département de physique, Université de Montréal, C.P. 6128, Succ.
Centre-Ville, Montréal, QC H3C 3J7, Canada; Claude.Carignan@UMontreal.CA
[3] Observatoire d'Astrophysique de l'Université de Ouagadougou (UFR/SEA), 03 BP 7021 Ouagadougou 03, Burkina Faso
[4] Department of Physics & Astronomy, Brandon University, Brandon, MB R7A 6A9, Canada; FosterT@BrandonU.CA

ABSTRACT

We present a new deep 21 cm survey of the Andromeda galaxy, based on high-resolution observations performed with the Synthesis Telescope and the 26 m antenna at the Dominion Radio Astrophysical Observatory. The H I distribution and kinematics of the disk are analyzed and basic dynamical properties are given. The rotation curve is measured out to 38 kpc, showing a nuclear peak at 340 km s^{-1}, a dip at 202 km s^{-1} around 4 kpc, two distinct flat parts at 264 km s^{-1} and 230 km s^{-1}, and an increase to 275 km s^{-1} in the outermost regions. Except for the innermost regions, the axisymmetry of the gas rotation is very good. A very strong warp of the H I disk is evidenced. The central regions appear less inclined than the average disk inclination of 74°, while the outer regions appear more inclined. Mass distribution models by ΛCDM Navarro–Frenk–White, Einasto or pseudo-isothermal dark matter halos with baryonic components are presented. They fail to reproduce the exact shape of the rotation curve. No significant differences are measured between the various shapes of halo. The dynamical mass of M31 enclosed within a radius of 38 kpc is $(4.7 \pm 0.5) \times 10^{11}\,\mathcal{M}_\odot$. The dark matter component is almost four times more massive than the baryonic mass inside this radius. A total mass of $1.0 \times 10^{12}\,\mathcal{M}_\odot$ is derived inside the virial radius. The spectral structure of the observations is very complex, with sometimes up to five H I components detected per spectrum, which is very rarely seen in other galaxies. New H I structures are discovered in the datacube. The most remarkable new features are an external arm and thin H I spurs in the disk outskirts. A relationship between these spurs and outer stellar clumps is evidenced. The external arm is 32 kpc long, lies on the far side of the galaxy, and has no obvious counterpart on the other side of the galaxy. Its kinematics clearly differs from the outer adjacent disk. Both these H I perturbations could result from tidal interactions with galaxy companions like NGC 205.

Key words: galaxies: fundamental parameters (mass) – galaxies: individual (M31, NGC 224) – galaxies: ISM – galaxies: kinematics and dynamics – galaxies: structure – Local Group

Online-only material: color figures

1. INTRODUCTION

In the last decade, several studies have contributed to the better understanding of the building history of the disk of the Andromeda galaxy (hereafter M31; Table 1), the most nearby massive spiral galaxy to the Milky Way (MW).

One of the most exciting result is probably the discovery of an extended stellar halo around M31 (Ibata et al. 2001). More and more studies are completing this new view of the stellar distribution of M31 and are revealing little by little the complex chemical, kinematical, and morphological nature of its halo (Ferguson et al. 2002; Reitzel & Guhathakurta 2002; Ibata et al. 2004, 2005, 2007; Brown et al. 2006, 2008; Guhathakurta et al. 2006; Kalirai et al. 2006a, 2006b; Martin et al. 2006; Faria et al. 2007; Majewski et al. 2007; Chapman et al. 2008). Basically, these authors find that the outskirts of the stellar disk are very clumpy and irregular, and the extended halo is a mix of many metal-poor and rich substructures like the southeastern Giant Stream (GS) and other seemingly shorter stream-like extensions, low-luminosity dwarf satellites and globular clusters, as well as an old metal-poor underlying (primordial?) halo which extends up to at least 150 kpc (in projection). These stellar tidal features and companion galaxies are the probable main imprints of the hierarchical growth of the M31 stellar disk and halo, like

the ones encountered in numerical models of dark matter evolution in the framework of the Cold Dark Matter (CDM) paradigm (e.g., Frenk et al. 1988; Klypin et al. 1999; Springel et al. 2005). Numerical models trying to explain the presence of the GS tidal debris around M31 propose a tidal interaction with a ~10^9 $\mathcal{M}_\odot$ galaxy progenitor (Fardal et al. 2006).

The gas content in the halo of M31 has also been probed recently from deep H I measurements, allowing the detection of a population of discrete low-luminosity clouds, with masses in the range of 10^5–10^7 $\mathcal{M}_\odot$ (Thilker et al. 2004; Westmeier et al. 2005). The authors suggest that those clouds could be the analogs of the high-velocity H I clouds seen around the MW (Wakker et al. 1999). They also suggest a manyfold origin of that gas (residual from galaxy merger or interaction, cooling flow in the Local Group, etc.), which may only contribute to ~1% of the total H I disk mass of M31. H I gas clouds from the intergalactic medium could thus also be the building blocks of M31.

At the same time, the advent of the new generation of X-ray, ultraviolet, and infrared space observatories allows to probe the structure of the interstellar medium of M31 with unprecedented details (Williams et al. 2004; Thilker et al. 2005; Barmby et al. 2006; Gordon et al. 2006; Stiehle et al. 2008). For instance, the mid-infrared images reveal a dominant ring-like distribution for the dust component. Its perturbed morphology seems to have been shaped by the passage of the companion Messier 32 through the M31 disk (Thilker et al. 2005; Block et al.

---

[*] Observations obtained at the Dominion Radio Astrophysical Observatory (DRAO), operated as a national facility by the National Research Council of Canada.

Table 1
Basic Optical Parameters of M31

Parameter	Value
Right ascension (J2000)[a]	$00^h42^m44\overset{s}{.}4$
Declination (J2000)[a]	$+41°16'08''$
Morphological type[a]	SA(s)b
Distance[b] (kpc)	785 ± 25
	$(1' = 229\ pc)$
Systemic velocity[a] (km s^{-1})	-300 ± 4
Optical radius[a], R_{25}	$95\overset{'}{.}3$
Inclination[c]	$77°$
Position angle[c]	$35°$
Total apparent B magnitude[c]	4.38
Corrected total B magnitude[d]	3.66
Absolute B magnitude	-20.81
Total blue luminosity	$3.1 \times 10^{10}\ L_\odot$
$(B-V)$[c]	0.91
$(U-B)$[c]	0.37
$(B-R)$[e]	1.37

Notes.
[a] de Vaucouleurs et al. (1991).
[b] McConnachie et al. (2005).
[c] Walterbos & Kennicutt (1987).
[d] $A_g = 0.33$, $A(i) = 0.8 \log(R_{25}) = 0.39$.
[e] Walterbos & Kennicutt (1988).

2006). A high-resolution kinematical survey of the molecular gas contained in the ring and spiral structures has also been presented (Nieten et al. 2006).

A large part of the H I studies that have been done on M31 go back up to ∼30 years ago (Guibert 1973; Emerson 1974; Newton & Emerson 1977; Cram et al. 1980; Unwin 1980a, 1980b; Brinks & Shane 1984). These data were acquired at low spectral and/or angular resolution data and did not necessarily cover the whole disk of the galaxy, mainly for sensitivity reasons. Another more recent H I study of M31 has been presented in Braun (1990) from Very Large Array (VLA) observations. Perhaps the most important result from all these studies is that the H I disk of M31 exhibits a warp whose effects are remarkable in the datacube by the presence of many spectral H I peaks along different line of sights. Another interesting result by Braun (1991) is the modeling of a rotation curve that appears to decline as a function of the galactic distance. A study of the mass distribution using this rotation curve only requires stellar bulge plus disk components, with no need of any dark matter halo. If it is really the case, M31 would be very different from every other spiral galaxy which is known to exhibit a flat rotation curve (or even increasing) at large galactocentric distances and thus to contain a massive hidden mass, unless the law of gravity is modified in these acceleration regimes (Milgrom 1983, 2008).

This result was the main motivation to get single-dish observations along the photometric major axis for the approaching disk half. Indeed, radial velocities of the H I gas in the receding side of M31 are contaminated by H I gas in the MW. We concluded that the outer H I rotation curve cannot be decreasing but seems remarkably flat at the largest radii (Carignan et al. 2006). However, since it was not possible to model the warp properly with those single-dish data, it was decided in 2005 to get full two-dimensional velocity information from wide-field synthesis observations at the Dominion Radio Astrophysical Observatory (DRAO).

In this paper, we present preliminary morphological, kinematical, and dynamical results obtained from the analysis of the DRAO H I observations. The direct objectives of this paper

are to present the most extended H I distribution of M31, to derive an accurate H I rotation curve in order to verify whether the rotation velocities really decrease at large galactocentric distances or really remain constant, as well as to derive its basic dynamical parameters.

It is worth mentioning here the very recent, wide-field and high-angular H I imaging presented in Braun et al. (2009) with the help of the Westerbork Synthesis Radio Telescope (WSRT) and Robert C. Byrd Green Bank Telescope (GBT). Future results from that very deep data set will surely serve as independent comparison with those we present in this paper and in other forthcoming papers from this series.

This paper is organized as follows. Section 2 describes the DRAO observations and the basic data reduction steps. Section 3 describes the line-fitting procedure as well as how the Galactic H I was subtracted from the datacube. Section 4 describes the H I content and distribution while Section 5 concentrates on the kinematics and on the calculation of the H I rotation curve. A comparison with results from different studies is also done in this section. An analysis of the perturbed outer regions of the disk is done in Section 7. Finally, a study of mass distribution models is done in Section 8. Concluding remarks are given in Section 9.

All velocities are given in the heliocentric rest frame and a Hubble's constant of $H_0 = 73$ km s^{-1} Mpc^{-1} is chosen throughout this paper (Spergel et al. 2007). Since the symbol R refers to as the galactocentric radius and most of the magnitudes and luminosities are given in the photometric R-band, no subscripts are attached to magnitudes or luminosities for clarity reasons, except where explicitly mentioned.

2. OBSERVATIONS AND DATA REDUCTION

2.1. H I Emission Line Observations

A total of five fields toward M31 were observed in the 1420 MHz continuum and 21 cm line with the Synthesis Telescope (ST) at DRAO between 2005 September and December. This interferometer consists of seven 9 m diameter antennae along an east–west baseline 617.1 m long. The primary beam of each element is $107\overset{'}{.}2$ (FWHM), and structures down to the resolution limit of $58'' \times 58''/\sin(\delta)$ in the 1420 MHz line are resolved within this beamwidth (a Gaussian taper to the u, v data is applied, broadening somewhat the synthesized beamwidth up from the nominal $49'' \times 49''/\sin(\delta)$ resolution in the continuum). Further instrumental details on the DRAO ST are found in Landecker et al. (2000).

Tables 2 and 3 list the observational parameters and field-of-view centers for the five individual aperture synthesis observations. Fields were chosen such that a spacing of $\Delta = 77'$ between centers was observed, giving nearly equal sensitivity over the whole area surveyed. The exposure times per field was 144 hr.

H I emission line images are made in each of the 256 channels across a 4 MHz bandwidth centered on $v = -300$ km s^{-1}. The spectrometer gives a resolution of 5.27 km s^{-1}, and each channel samples a width of $\Delta v = 3.3$ km s^{-1}. The H I line datacube spans 843 km s^{-1}. The theoretical noise at the pointing center is $1.75 \sin(\delta)$ K, corresponding closely to the measured values in Table 3 (for channels free from H I emission).

To depict structures accurately in the radio continuum and H I line images (especially those of angular size $\geqslant 56'$, missed by the interferometer due to its shortest baseline limit of 12.9 m), low spatial frequency information is routinely added to each

Table 2
Observational Parameters of the DRAO Aperture Synthesis Observations of Messier 31

Parameter	Value
Observation dates	2005 September–December
Total length of observation	144×5 hr
Velocity center of band	−300 km s^{-1}
Total bandwidth	4 MHz (843 km s^{-1})
Number of velocity channels	256
Frequency sampling	15.6 kHz
Velocity resolution	5.3 km s^{-1}
Number of spatial pixels[a]	1024
Pixel angular size[a]	22$''$

Note. [a] Values given for the full resolution initial datacube.

Table 3
DRAO Synthesis Telescope Observational Set-up and Noise

Obs. Date (2005)	Field Center Coordinates (J2000, h:m:s,°:$''$:$'$)	Beam Parameters $\theta_{maj}('){\times}\theta_{min}(')$ and Orientation (°)	Noise at Field Center (K)
Oct 5	0:52:19.7, 43:15:00	1.46 × 0.98, −90.2	1.12
Sep 9	0:47:32.0, 42:19:00	1.50 × 0.98, −90.2	0.98
Sep 9	0:42:44.3, 41:16:09	1.53 × 0.98, −90.0	0.83
Nov 4	0:37:56.6, 40:08:00	1.58 × 0.97, −89.8	1.04
Dec 10	0:33:18.9, 39:00:00	1.57 × 0.97, −87.2	1.06

Notes. Summary of 1420 MHz line + continuum observations centered on and surrounding Messier 31. Noise is indicated for the full resolution initial datacube.

ST map. These "short-spacing" data are obtained from H I line observations made with the DRAO 26 m paraboloid (Higgs & Tapping 2000). The flux is corrected for stray radiation entering through the sidelobes, and the continuum is subtracted from all channels before the integration with the ST observations. The spatial resolution of these data is 37$'$×35$'.3$; all spectrometer settings were the same as for the ST data.

2.2. Data Reduction and Mosaicing

Prior to mosaicing our five fields together, we perform some standard data processing steps (processing methods are similar to those developed for the Canadian Galactic Plane Survey (CGPS), described in Taylor et al. 2003). First, a continuum baseline level is removed from each datacube. Average emission-line-free channels at both the low and high velocity ends of the cube are made, and a linear interpolation (determined from these two continuum maps) is then subtracted from each channel map in the datacube. To calibrate the flux scale of each cube, we compare point sources in the average of the two continuum end-channels to those in the 30 MHz continuum band map of each field (these maps are first CLEANed around the strongest sources). This can be done since continuum maps are flux calibrated against several strong sources that are routinely observed by the ST (e.g., 3C 48, 3C 286; see Table 1 of Taylor et al. 2003, for sources and fluxes). An error-weighted mean of the flux ratio $S_{1420cont}/S_{H Icont}$ for all point sources above a cutoff level (20 mJy beam^{-1}) is obtained; this sample is further trimmed by rejecting sources ±0.5 away from the mean. Typically, 20–30 sources remained in the sample for each field. The uncertainty in the flux calibrated this way is ∼5%.

The processed fields are combined into a 1024 square pixels mosaic, centered on optical coordinates R.A. = 00^{h}42^{m}44^s.3, Decl. = +41°16$'$09$''$ (J2000). The pixel size is 21$''.875$. The central 93$'$ radius of the primary beam constitutes the final width of the five individual fields, which were mosaiced together. The final mosaic spans 515$'$ oriented along M31's disk. The final noise values for the mosaic (measured) are ΔT_b ∼0.85 K in the individual field centers, and ΔT_b ∼ 0.95 K in the overlapping regions.

The final step consists in merging interferometer data with single-dish (26 m telescope) observations. For simplicity, this merging is performed in the map plane (as opposed to the u, v visibilities plane, as is done for the CGPS; see Taylor et al. 2003) using the procedure described below. The interferometer mosaic is first convolved to the resolution of the single-dish mosaic; this is then subtracted from the 26 m mosaic. The resulting difference map should contain H I structures invisible

to the interferometer, so it is added back to the full-resolution ST mosaic. This procedure gives equal weight to low and high spatial frequency structures, and while it is somewhat different from the method used in the CGPS (where a tapering function weights the overlapping spatial frequencies of both maps), the results of both approaches are very similar for H I line images.

A spatial binning of 2 × 2 pixels is finally applied to the datacube in order to decrease noise in the spectra. The datacube has a final dimension of 512 × 512 pixels, with a pixel size of 43$''.75$. This angular sampling is well sufficient for the kinematical and dynamical purposes. It corresponds to 167 pc at the distance of 785 kpc. The DRAO synthesized beam size of ∼60$''$ × 90$''$ samples a linear scale of ∼230 × 340 pc in the H I disk of Messier 31. It is as resolved as a typical H I mapping of 10 Mpc distant disks observed with a high-resolution beam resolution of, e.g., 5$''$. The present H I observations can thus be considered as high-resolution ones and for this reason no correction for beam-smearing is needed.

3. H I DATACUBE ANALYSIS

3.1. Previous Works

H I spectra of Messier 31 are known to exhibit multiple peaks in emission (e.g., Newton & Emerson 1977; Cram et al. 1980; Bajaja & Shane 1982). It is also the case in molecular gas observations (Dame et al. 1993; Loinard et al. 1999; Nieten et al. 2006). For the H I data, this is particularly well illustrated along position–velocity (PV) diagrams made parallel to the major axis in Cram et al. (1980) or Brinks & Burton (1984), where a second velocity peak is seen in addition to the main (brighter) peak. Both these lines draw a tilted figure-eight shape in which the main peak traces the usual rotating pattern of the disk (steep velocity rise in the inner regions sometimes accompanied by a flatter velocity part in the external regions) and the second peak shows a linear (shallower) velocity rise all along the slices.

With the noticeable exceptions of Brinks & Shane (1984), Brinks & Burton (1984), or Braun (1991), the previous H I studies of M31 analyzed their data with a single emission line approximation in order to derive an integrated emission map, a velocity field, or a rotation curve. For instance, Newton & Emerson (1977) reported that when two peaks are detected, the radial velocity of the spectrum is chosen at the barycenter of the lines. Though it seems a reasonable hypothesis in regard to the low spectral resolution of all these old observations, it surely provides a biased velocity distribution for M31. Integrated fluxes and velocities are incorrectly estimated when lines are blended.

A simple explanation for the origin of the two components comes from the fact that the H I disk of Messier 31 is warped at
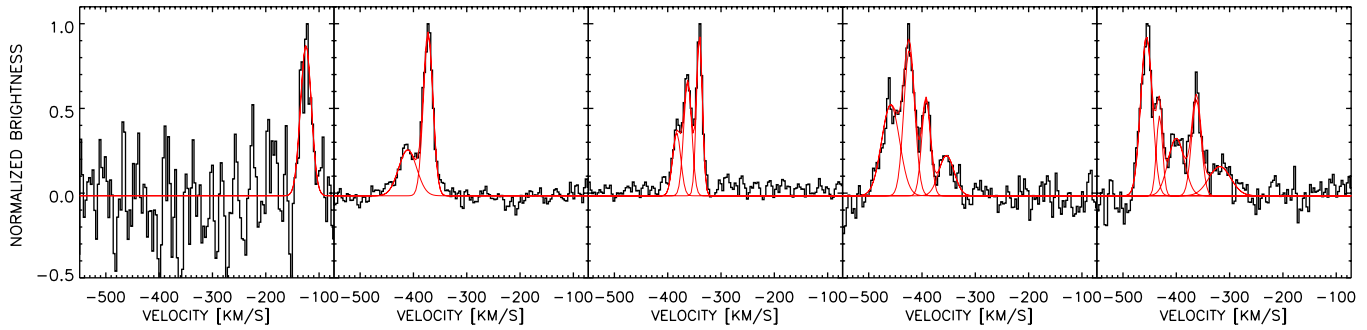
Figure 1. Selected M31 spectra from the H I datacube showing multiple H I peaks and fitted components (red solid lines).
(A color version of this figure is available in the online journal.)

large galactocentric radius. Because the disk is highly inclined, the projection effects enable us to cross two times the disk along the line of sight (H I gas is supposed to be optically thin). The line-of-sight velocities are thus composed of a main H I component lying in the internal disk region in addition to a secondary component lying in the external warped region of the disk but seen projected at small radii. The presence of the warp were the reasons that led Brinks & Burton (1984) to analyze the WSRT data differently from the other studies by a warped and flaring H I layer model. They proposed two velocity fields, one for the disk and another one for a separate, external warped structure. From this, they deduced that about 39% of the total H I mass of the disk could reside beyond 18 kpc, in its warped region.

3.2. Current Analysis

3.2.1. Evidence for Multiple H I Spectral Components

A provisional study of the DRAO datacube has been presented in Carignan et al. (2007) where moments maps were derived by fitting a single Gaussian to each spectrum of the datacube. We extend here this simplistic view of our data to a more detailed analysis where multiple H I components are now fitted to the spectra. The high-sensitivity observations indeed reveal a new more complex view of the neutral gas in M31 than what has been shown in past H I studies. Figure 1 displays several H I spectra picked at different positions through the datacube. The H I spectra exhibit almost all the time more than one component, sometimes up to five peaks. This result confirms the basic view shown in, e.g., Brinks & Burton (1984) where two H I components are shown (and sometimes more), but largely extends the detection of new multiple spectral components in the datacube. One clearly wants to emphasize here that a single or two peak analysis cannot apply straightforwardly to the current data. This would provide biased intensity, velocity, and velocity dispersion maps.

3.2.2. Contamination by the Milky Way

A usual problem with observations of M31 is the contamination from the MW. M31 is so massive that its receding half can reach radial velocities that coincide with those of the Galaxy. However most of Galactic H I remains relatively easy to detect and to model because its lines can be observed almost everywhere in the field of view (Figure 2). We detect two major Galactic lines. A first bright component is found at -4 ± 2 km s^{-1} for a velocity dispersion of 6 ± 3 km s^{-1} as deduced from 66,000 spectra. This line does not contaminate the emission from Messier 31 due to its too high radial velocity. Another line is found at -40 ± 11 km s^{-1} for a velocity dispersion of
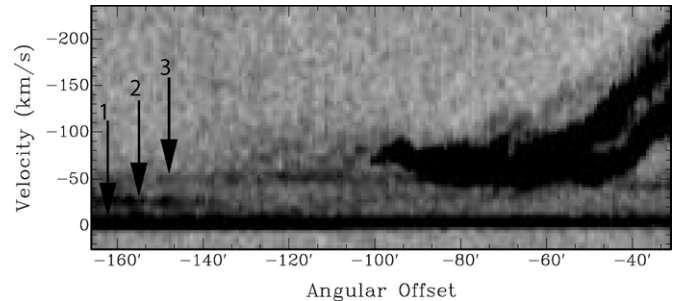

Figure 2. Contamination of the data by Galactic H I. The slice through the datacube shows three H I components from the Milky Way at (1) ~ -4 km s^{-1}, (2) ~ -20 km s^{-1}, and (3) ~ -40 km s^{-1}.

18 ± 10 km s^{-1}, as deduced from 19,500 spectra free from M31 H I emission. This is the line that mostly contaminates the NE half of M31. Another minor MW line is observed around -20 km s^{-1} (see Figure 2). This emission line does not contaminate the signal from M31 because of its high radial velocity. Other very faint lines only revealed by very high contrast imaging are found around -70 km s^{-1} and -90 km s^{-1}. Their contribution to the whole emission is very negligible.

The method used to subtract the MW emission from the datacube is similar to the one employed by Braun et al. (2009). For each channel map, a mask containing pixels with H I emission of M31 is first created. The mask covers a small fraction of the field of view and allows to blank the H I emission of M31. A two-dimensional model of the Galactic emission is then generated by fitting a third-order two-dimensional polynomial to the blanked channel map. The two-dimensional model is then subtracted from the initial channel map. This method allows to remove most of the galactic H I. Residual MW contamination is removed by hand during the cleaning of the multiple velocity fields (see Section 3.2.3). We tried another approach to remove MW H I by simultaneously fitting Gaussian lines in addition to H I from M31. However, that subtraction method had to be rejected because too many negative residuals are created in the cube, introducing artificial local minima in the integrated emission map.

As claimed in Braun et al. (2009) it is very difficult to define whether small-scale H I structures observed around the disk of M31 are bound to Andromeda or simply Galactic cloudlets. For simplicity reasons, we decide to ignore the gas emission out of the main disk in the following analysis.

There is no clear mention in older H I studies of M31 of Galactic emission around ~ -40 km s^{-1}. It is thus possible that measurements of the H I flux and velocity dispersions are overestimated for the receding half of the disk in those
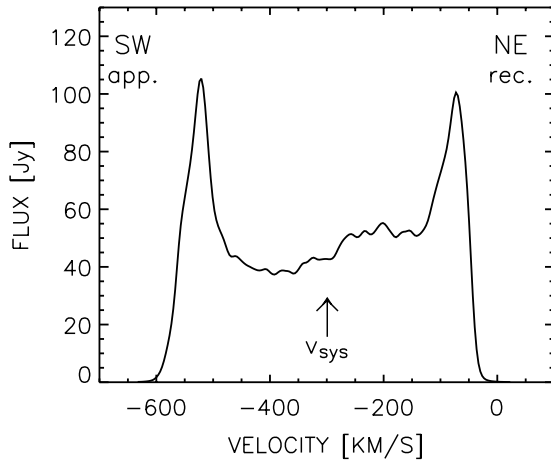
Figure 3. H I integrated profile of Messier 31. v_{sys} refers here to as the integrated weighted mean systemic velocity derived from the profile.

works. However, their velocity fields remain very marginally contaminated.

### 3.2.3. Emission Line Detection and Fitting

The detection of emission lines is done by keeping all channels above a 3σ level, where σ is the intensity dispersion derived from half of the spectrum. This dispersion measurement is justified by the fact that most of the channels are free from H I emission. The method to locate a peak in the remaining channels is a usual slope computation technique. An emission line is detected when the slope sign does not change along at least two consecutive channels, as measured both to the left and right sides of a peak. Once detected, velocities and amplitudes of these peaks serve as initial guesses for the minimization step where Gaussian profiles are fitted to the spectrum. A "continuum" value is fitted as an additional parameter as well. It is very close to zero because a baseline has been subtracted in each pixel during the data reduction (see Section 2.2). Boundary constraints are applied to the parameters (amplitude, velocity centroid, and dispersion). A velocity centroid has to be fitted within the observed spectral range, a velocity dispersion has to be greater than one channel width and lower than an artificial (unexpected) large value of 130 km s^{-1}, and a peak amplitude has to be greater than zero and lower than the highest intensity observed in a spectrum. Results of spectral fittings of 1–5 H I components are displayed in Figure 1.

A final cleaning step is then applied to the data. All fitted lines whose amplitude is larger than a threshold of 3σ were kept. All lines whose velocity dispersion is greater than 60 km s^{-1} are discarded because such high values turn out to be very rare and, above all, unrealistic. Obvious residuals of MW emission are also removed from the different maps. As a result of this filtering procedure, among the 25,350 available spectra in the H I datacube and in which at least one component is detected with a signal-to-noise ratio of at least 3, two peaks are detected in $\sim$66% of them, three peaks in $\sim$35% of them, four peaks in $\sim$14% of them, and five peaks in $\sim$3% of them. A large number of H I components (>3 peaks) is therefore rare in the datacube.

4. H I DISTRIBUTION AND KINEMATICS

4.1. Integrated Properties

The flux in each individual channel was summed to give the global H I profile of Figure 3. The profile is relatively regular.
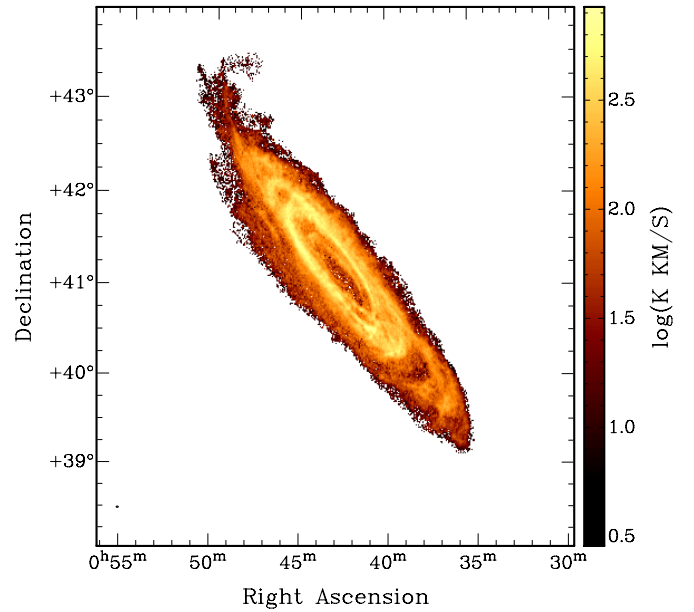
Figure 4. Total H I distribution of Messier 31. The small ellipse in the bottom-left corner displays the angular size of the synthesized beam ($\sim$1′ × 1′.5).

(A color version of this figure is available in the online journal.)

The two peaks are almost perfectly symmetric. An asymmetry is nonetheless observed between them. There is more gas in the receding side of the galaxy than in its approaching part. An intensity-weighted systemic velocity of -299 ± 3 km s^{-1} and a midpoint heliocentric radial velocity of $v = -297 \pm 3$ km s^{-1} are derived. The measured profile widths at 20% and 50% levels are $W_{20} = 533 \pm 3$ km s^{-1} and $W_{50} = 509 \pm 3$ km s^{-1}. This can be compared to the RC3 (de Vaucouleurs et al. 1991) values of $v = -300 \pm 4$ km s^{-1}, $W_{20} = 536 \pm 7$ km s^{-1}, and $W_{50} = 510 \pm 7$ km s^{-1}, which show a good agreement with ours within the errors.

The integrated flux of 29221.4 Jy km s^{-1} implies a total H I mass of $4.23 \times 10^9 \, \mathcal{M}_\odot$. This mass is larger by 15% than the one measured in Brinks & Burton (1984), is comparable with the estimate by Cram et al. (1980) and is smaller by 25% than the one derived in Braun et al. (2009; before opacity corrections). The difference between all mass estimates is likely due to the various sensitivities of the observations and to the accuracy of the subtraction of the contaminating MW emission.

4.2. The Three-dimensional Structure of M31

Figure 4 displays the total H I integrated emission of M31 and a three-dimensional view of the datacube is shown in Figure 5. The lowest H I column density of the DRAO observations at a 3σ peak detection level is $\sim$1.7 $\times 10^{19}$ cm^{-2} and the highest H I column density is $\sim$5 $\times 10^{21}$ cm^{-2}. The maximum disk extent is $R \sim 2°.6$ ($R = 36.4$ kpc), as derived along the photometric major axis. It corresponds to 1.67 R_{25} and 6.48 R_d, with R_d being the stellar disk R-band scale-length derived in Section 8.2.1.

The high-resolution H I map reveals a disk with very little gas in its central regions, a feature usually observed in early-type disks. Two ring-like structures are observed around $R \sim 10'$ (2.5 kpc) and $R \sim 20'$–25′ (4.6–5.7 kpc). We refer to them as R1 and R2 in Figure 5. At such high inclination it is difficult to firmly claim whether they are real rings like, e.g., those created by gas accumulation at the location of inner or ultra-harmonic Lindblad resonances, or tightly wound spiral arms.
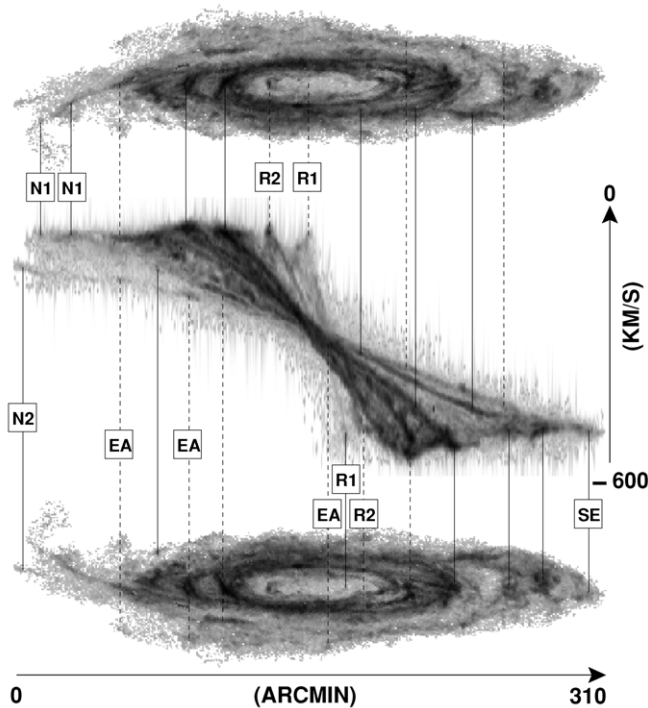
Figure 5. Three-dimensional view of the H I datacube of M31. The middle panel is the position–velocity diagram of the *whole* datacube projected on the photometric major axis, which is aligned along the horizontal axis. The bottom panel is the total integrated H I image. The top panel is the mirror image of the bottom panel. The solid (dashed) lines are for H I emission from the front (respectively far) side of the galaxy. Labels N1, N2, SE show the two northern H I spurs and the southwestern extension, EA the external arm, R1 and R2 the ring-like structures in the center of the disk (see the text for details, Section 4.2).

They are coincident with dusty ring-like structures observed in NIR images from *Spitzer*/Infrared Array Camera (IRAC) data (Barmby et al. 2006) as well as with molecular gas ring-like structures (Nieten et al. 2006). Another wider bright ring-like structure is observed for $40' < R < 80'$ (9.1–18.3 kpc). Though it is often referred to as the "10 kpc ring" of M31, its morphology is more complex than a regular ring because holes are observed in it as seen, e.g., in the approaching side of the disk. Long spiral arms are then clearly seen at large radii. The most prominent spiral arm of M31 is observed in the southwestern half of the disk.

A faint external spiral arm (label "EA" of Figure 5) is discovered on the edge of the receding half of the disk (southern part of the NE quadrant of Figure 4). It is connected to the long spiral arm which arises from the SW and its apparent end is clumpy (see region around $\alpha_{2000} = 00^h49^m41^s80$, $\delta_{2000} = +42^d12'54''$). Other new structures that were not seen in old H I data are the two disk extremities to the SW and NE (labels "SE" for southwestern extension and "N1"/ "N2" for northern spurs in Figure 5). Here thin and faint gaseous extensions are observed. Their gas distribution and kinematics are discussed in more details in Section 7.

The top and bottom panels of Figure 5 is the right ascension–declination view of the datacube while the middle panel is a rotation of this later by 90° with respect to the horizontal axis (disk photometric major axis). It is thus a position velocity plot of the whole datacube projected onto the major axis. Vertical lines are drawn to guide the eye in order to link the kinematics to the spatial distribution of the H I gas. The main features of the diagram are as follows.

1. All spiral- and ring-like structures do not cross at the same location in the center of the diagram ($v = -300$ km s^{-1}). This is probably caused by a lopsided nature of the disk.
2. Except for the external arm (EA), all spiral- and ring-like structures have a symmetric counterpart with respect to the galaxy center. This symmetry is not regular in velocity amplitude within $\sim 50'$ around the center, as seen for instance with the velocity peaks of the ring-like structure R2. This is also caused by the disk lopsidedness, as well as other probable noncircular gas motions in the central parts.
3. A steep velocity gradient is observed in the innermost ring-like structure (R1).
4. The northern spur N2 appears as a kinematical extension of the external arm in the velocity space.

The neutral gas distribution of the DRAO observations is consistent with H I images from many other works (Cram et al. 1980; Roberts & Whitehurst 1975; Bajaja & Shane 1982; Emerson 1974; Brinks & Shane 1984). The agreement is better with the deep WSRT observations of Braun et al. (2009) because of the comparable sensitivity with the DRAO observations. Their H I image do show the external arm as well as the northeastern spurs and southwestern extension. It thus leaves no doubt about their presence in the disk outskirts of M31.

The gas distribution for all detected H I components is shown in Figure 6. In each pixel, the components are displayed by decreasing integrated emission from left to right. A brief discussion on the origin(s) of all these H I peaks is proposed in Section 6.

5. KINEMATICAL ANALYSIS

In Brinks & Burton (1984), a three-dimensional model of WSRT observations was presented in order to reproduce the complex structure of the datacube. They proposed a flared and warped disk model for M31 that can explain the presence of double H I peaks observed in most of pixels. Not all of the dozen free parameters of their model are directly fitted to the datacube. Some assumptions deduced from the observations had to be made. For instance, the modeled rotation curve they use and that comes from the bulk velocities observed along the photometric major axis is flat all through the inner disk (except in the central regions), with a maximum velocity of ~ 250 km s^{-1}. Another three-dimensional model derived from the same WSRT data and H I observations of Emerson (1974) is presented in Braun (1991). It describes the gas and velocity structures in terms of spiral density waves and shows a central disk which is tilted by $\sim 15°$ from the median plane of the galaxy. Modeled position velocity diagrams reveal a complex velocity structure (see Figure 5 of Braun 1991).

A complete three-dimensional analysis of the DRAO datacube taking into account both a warped and flaring disk, with spiral and/or other density waves, in addition to other processes like, e.g., a lagging halo, as observed in other galaxies (Fraternali et al. 2001, 2002; Barbieri et al. 2005; Oosterloo et al. 2007), is beyond the scope of this paper that aims at presenting preliminary dynamical results from more simple geometrical and kinematical hypothesis. We only analyze the kinematics of the bulk rotation of M31 by fitting a tilted-ring model to a velocity field, similarly to what is usually done in many other extragalactic studies. The inclination of the disk is very well suited for such a model because the degeneracy between the rotation velocity and the inclination is small around 75° (Begeman 1989).
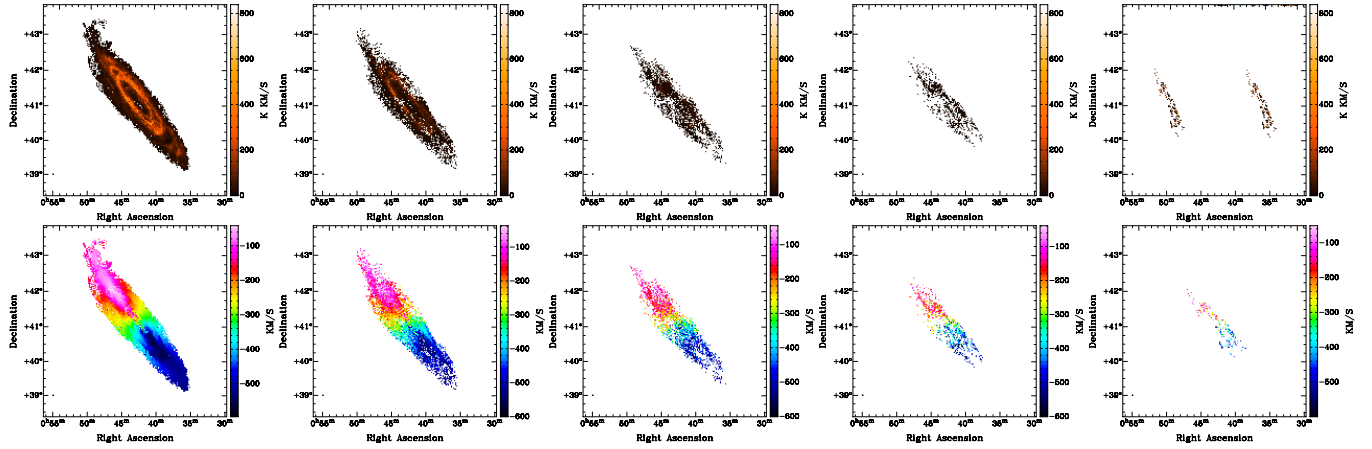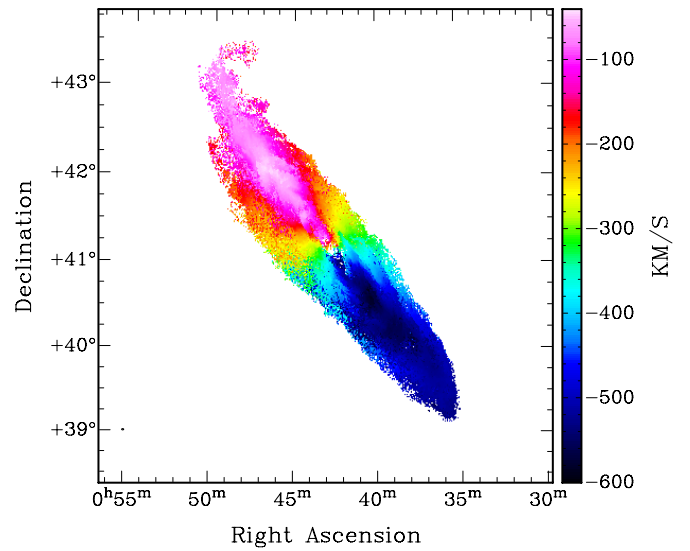
Figure 6. H I integrated emission and velocity maps of M31. The H I components are sorted by decreasing brightness from left to right.
(A color version of this figure is available in the online journal.)
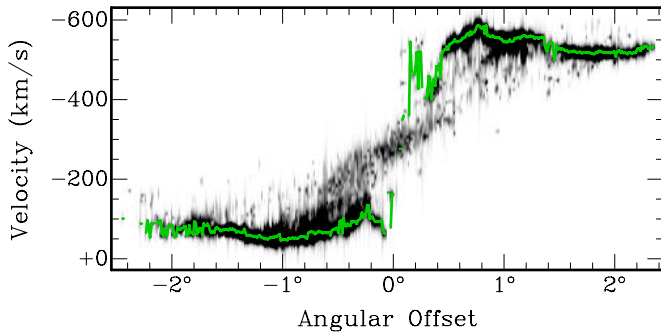
Figure 7. Position velocity plot made along the photometric major axis P.A. = 38°. A green curve represents a slice through the velocity field of the main H I component.

(A color version of this figure is available in the online journal.)

Figure 8. Velocity field of M31 used for the titled-ring model analysis.
(A color version of this figure is available in the online journal.)

Probably the major ambiguity with our analysis comes from that it seems difficult to decide for pixels that exhibit more than one peak which of the spectral components is the best tracer of the bulk disk rotation. Several methods can be applied to sort the different lines and build a useful velocity map. For instance, lines can be sorted by their amplitudes, integrated fluxes, velocity centroids, or widths. There is generally one line whose peak amplitude or integrated intensity strongly dominates the spectrum. However, choosing the brightest peak for the bulk rotation such as what is shown in Figure 6 remains problematic in pixels where the H I emission is dominated by other structures than the bulk disk (like extraplanar gas) or when the projection effects contaminate the emission. In particular, the H I emission in the central regions is dominated by gas from the warped part of the disk. This is illustrated in the position velocity plot made along the major axis of the galaxy (Figure 7; see also Brinks & Burton 1984). The steep innermost gradient of the faint central ring-like structure is dominated by the shallow linear emission from the warped gas. Choosing this brightest later line would lead to discontinuities in the velocity field and thus to an erroneous inner rotation curve. For each pixel a good compromise is to select the component that has the largest velocity relative to the systemic velocity of the galaxy while avoiding isolated faint features. It permits rejection of the bright component from that shallow linear emission, which is closer to the systemic velocity, and the components beyond the flat part of the PV diagram, which come from possible extraplanar gas

(e.g., high-velocity clouds). The velocity field that is generated following that method is shown in Figure 8 and a velocity cut along its major axis is reported in Figure 7 as a green line. That map probably allows to obtain the best velocity continuity with no three-dimensional model of the datacube. Hereafter, we refer to the "main component" the H I line that has been chosen to derive this velocity field. The mass attached to the main component is $2.49 \times 10^9 \, \mathcal{M}_\odot$.

5.1. Tilted-ring Model

The kinematical parameters and rotation curve are determined by fitting a tilted-ring model to the velocity field following the procedure described in, e.g., Verheijen & Sancisi (2001) or Chemin et al. (2006). Briefly, the *rotcur* task (Begeman 1989) of the GIPSY data reduction software (van der Hulst et al. 1992) is used to fit the variation of kinematical parameters as a function of radius. It is considered here that gas motions are along circular orbits. Hence, no axisymmetric radial motions (gas inflow or outflow) or vertical motions perpendicular to the galaxy plane are derived so that sky plane velocity $v_{\rm obs}$ can be written as the projection of the only rotation velocity along the line-of-sight

$v_{\rm obs} = v_{\rm sys} + v_{\rm rot}\cos(\theta)\sin(i)$. Here, θ is the azimuthal angle in the galactic plane, i is the inclination, and $v_{\rm sys}$ is the systemic velocity of M31.

In the innermost regions of the disk the largest radial velocities are mostly *not* detected around the (photometric) major axis but at $|Y| > 0$. As a consequence we decided to use the full velocity field to do the tilted-ring model analysis. We have verified that the basic results are not affected by the choice of the opening angle around the major axis by comparing with results obtained using a smaller angle (half-sector of 30° instead of 90°). As expected, the parameters derived using the full coverage of the kinematics are better constrained and the rotation curve is probed more deeply toward the galaxy center for the large opening angle than for the small one. The shape of the rotation curve is unaffected by the opening angle.

Note however that a $|\cos(\theta)|$ weight is applied to the data points during the fitting, giving less weight to pixels close to the minor axis. This is because the contribution of $v_{\rm rot}$ to the line-of-sight velocities is less important along the minor axis (see also Begeman 1989; de Blok et al. 2008).

One has to note that the NE spur "N2" and the external arm have been masked for the tilted-ring model analysis because their kinematical properties make them not linked to the disk or the other adjacent spur-like structure (see Figures 5 and 14, and Section 7). Leaving them in the velocity map would add large scatter in the results as well as a fail of the tilted-ring model at some outer radii.

The location of the dynamical center and systemic velocity $v_{\rm sys}$ are first fitted to the velocity field by keeping the disk inclination i and position angle of the kinematical major axis P.A. fixed at the photometric values ($\sim 75°$ and $\sim 38°$, respectively). The fitted systemic velocity of M31 is $v_{\rm sys} = -304.5 \pm 6.8$ km s^{-1}, whose value is in very good agreement with what is found using the integrated spectrum (Section 4). The location of the dynamical center is found to be offset from the photometric center by ~ 0.55 kpc (in projection). However, the dispersion around that location is ~ 0.68 kpc (in projection), showing that this offset is not really significant.

Then the variation of i, P.A., and $v_{\rm rot}$ are measured. The position angle is generally very well constrained with small uncertainties (see the top panel of Figure 9). It can be fixed in a next step to fit the inclination and the rotation curve. The radial profiles of i and P.A. sometimes display ring to ring wiggles that may look artificial (Figure 9). This is the reason why the smoothed profiles are used to derive the rotation curve in a final step. Model velocity and residual velocity maps are then generated. The fitting of the parameters and rotation curve is repeated until a minimum is found for the average and scatter of the residual map.

5.2. Major Axis and Inclination Variations

Figure 9 displays the observed and smoothed profiles of P.A. and i and Table 4 lists the parameters.

We identify five distinct regions in the profiles. First there is a central region $R \lesssim 27'$ where the inclination (position angle) strongly increases as a function of radius by $\sim 40°$ (10°, respectively). Then a bump is observed between $27' < R \lesssim 62'$ for the position angle which reaches its maximum at $R = 45'$ (P.A. = 39°). Then an extended region between $62' < R \lesssim 120'$ where a very small increase of position angle is detected while the inclination remains remarkably constant around 74°. Between $120' < R \lesssim 145'$ a dip both in the inclination and position angle profiles is detected. The inclination drops down
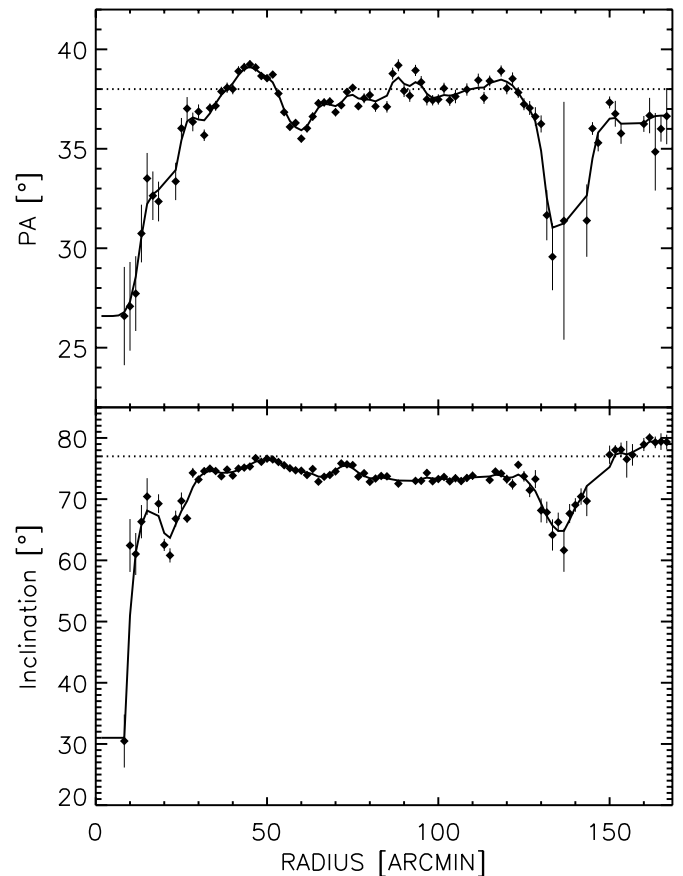
Figure 9. H I disk inclination and position angle of the kinematical major axis as determined from tilted-ring models to the H I velocity field of Messier 31. The dashed curves represent the smoothed models of i and P.A. used to fit the rotation velocities. Horizontal dotted lines show the photometric values.

to 61° and the position angle to 29°. Note that the uncertainties are larger in that radial range. Finally, beyond $R = 145'$, the position angle remains constant while the inclination is observed to slightly increase toward larger values from 77° to 80°. The average H I disk inclination is $(74°.3 \pm 1°.1)$ and the average H I disk position angle is $(37°.7 \pm 0°.9)$, as measured for $27' < R \lesssim 120'$ (from 6 kpc to 27 kpc). In that radial range, the kinematical inclination is therefore by 3° lower than the one derived with optical surface photometry.

5.3. The H I Rotation Curve

The H I rotation curve of M31 is shown in Figure 10. Its velocities are listed in Table 4. The rotation curve is very peaked in the innermost regions, showing velocities up to $v_{\rm rot} = 340$ km s^{-1}. Here, the asymmetry between both disk halves is prominent. A velocity dip is then observed at $R = 18'.3$ (4 kpc). The rotation curve is then observed to increase up to $v_{\rm rot} = 267$ km s^{-1} at $R \sim 47'$, to remain roughly flat between $47' \lesssim R \lesssim 75'$ ($v_{\rm rot} = (264 \pm 4)$ km s^{-1}), to decrease down to ~ 230 km s^{-1}, to remain flat between $95' \lesssim R \lesssim 120'$ ($v_{\rm rot} = (230 \pm 4)$ km s^{-1}) and finally to increase up to $v_{\rm rot} = 275$ km s^{-1} in the outermost regions.

The uncertainties on the rotation velocities are derived as follows. If gas rotation is made on purely axisymmetric and circular orbits, then rotation velocities are exactly the same at opposite sides of the galaxy. If the disk is perturbed, then the axisymmetry is usually broken and differences between rotation velocities of the approaching and receding halves exist.
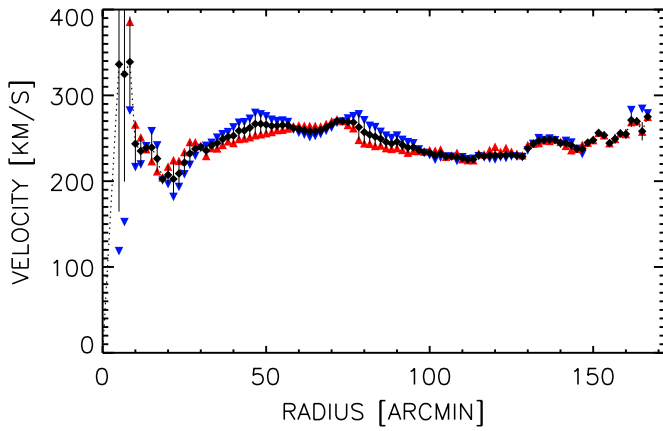
Figure 10. H I rotation curve of Messier 31. The filled diamonds are for both halves of the disk fitted simultaneously while blue downward/red upward triangles are for the approaching/receding sides fitted separately (respectively).

(A color version of this figure is available in the online journal.)

Figure 11. Comparison between H I rotation curves from Newton & Emerson (1977; crosses), Brinks & Burton (1984; filled circles), Braun (1991; open triangles), Carignan et al. (2006; filled diamonds), and our new derived rotation curve (solid line).

We thus choose a definition of velocity uncertainties that also takes into account this effect. Uncertainties are indeed defined as the quadratic sum of the formal 1σ uncertainty from *rotcur* with the maximum velocity difference between rotation curves (both disk sides model values derived simultaneously minus the approaching or receding side model values derived separately, weighted by the number of points in each side). With this definition, each uncertainty is generally larger and more conservative than the very small one derived with *rotcur*. It draws a better representation of any departure from axisymmetry. As a result the largest uncertainties are observed in the central regions. Elsewhere the uncertainties on the rotation velocities are very small, generally lower than 10 km s^{-1}. It shows the robustness of the method used to select lines to create the velocity field. Note that for some of the annuli beyond $R = 148'$ velocities could only be derived for the receding half. At those radii, the uncertainty is fixed at the formal 1σ error provided by *rotcur*.

5.4. Comparison with Other Works

5.4.1. The Rotation Curve

Figure 11 displays several previous H I rotation curves of M31 (Newton & Emerson 1977; Brinks & Burton 1984; Braun 1991; Carignan et al. 2006) and our new result. The agreement with our previous result (Carignan et al. 2006) is not good between 15 kpc and 23 kpc. This difference can be explained by the fact that Carignan et al. (2006) used a single emission line approximation while deriving the velocity field from low-resolution H I data of Unwin (1983). In the external parts the curves are in better agreement. The curve of Carignan et al. (2006) is flat at these radii, whose feature is not observed anymore. This is likely due to the assumption of constant position angle and inclination in our previous study. The agreement with the data points from Newton & Emerson (1977) looks better. Except for $R < 3$ kpc and for some points between $7\,\text{kpc} < R < 16$ kpc, the agreement with the curve of Braun (1991) is not good. The low velocities he measures around 15 kpc and at large radius (down to $v_{\text{rot}} = 190$ km s^{-1}) cannot be reproduced from the tilted-ring analysis. The origin of this discrepancy may be due to different choices of velocity components to extract the velocity fields. The agreement with the model of Brinks & Burton (1984) is good within $4 < R < 15$ kpc and poor beyond 19 kpc because the rotation curve is not flat throughout the whole disk.
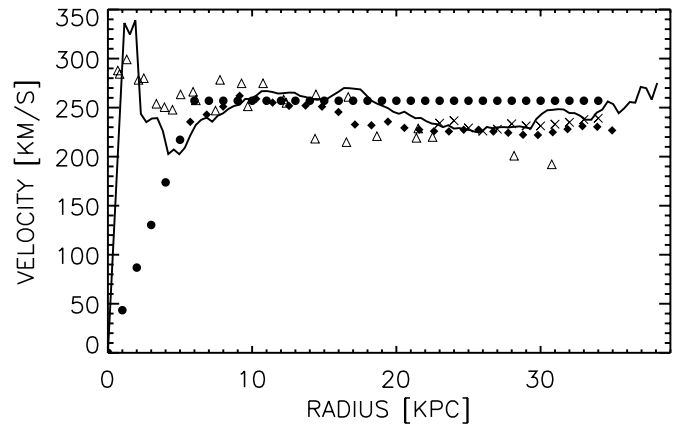
5.4.2. The Warp of M31

Results shown in Figure 9 imply the presence of two warps in M31. The first warp is located in the central parts ($R \lesssim 6$ kpc) where the disk orientation appears less inclined by $\sim 10°$ (in average) than the disk. The dip at 4 kpc thus corresponds to perturbed motions located in the inner warped disk. The nuclear region ($R < 2$ kpc) is even more perturbed as it behaves like a "warp in the warp." Here rotation velocities, inclination, and position angles are very different than anywhere else in the disk. Gas is observed to be very close to face-on. The very large uncertainties on the rotation velocities show that noncircular motions may be very important here. A second warp is detected in the outer parts ($R > 27$ kpc), where the disk is surprisingly oriented like in its inner warped part (P.A. and inclination) and then becomes more and more inclined at the largest radii. The fact that H I gas is observed to start rotating faster where the outer warp appears is also probably a consequence of the inferred perturbed orbits. Note however that the symmetry is excellent between both halves whereas it is not the case in the inner warp.

This is not the first time that warps are evidenced in M31. One can mention results by Ciardullo et al. (1988) and Braun (1991) for the inner regions, and Newton & Emerson (1977), Henderson (1979), or Brinks & Burton (1984) for the outer regions.

1. Braun (1991) showed that the H I distribution is tilted by $15°$ in the inner $10'$ (2.3 kpc). We confirm the presence of the inner H I warp in the DRAO observations. It is actually observed to extend up to $R = 6$ kpc for a maximum tilting angle of $\sim 15°$ and a maximum twisting angle of $\sim 7°$ with respect to the average disk inclination and position angles as given above. If the perturbation in the nuclear region is genuine, then the warp is even more prominent, with maximum tilting and twisting angles of $42°$ and $10°$.

2. The ionized gas distribution is more circular in the bulge, implying a more face-on disk (Ciardullo et al. 1988). Our measurement confirms this trend.

3. Newton & Emerson (1977) derived warp parameters in the outer disk ($R > 28.5$ kpc, or $125'$), with a decreasing position angle (down to $30°$) and an increasing inclination (up to $83°$). The shape, amplitude, and location of the outer warp detected in the DRAO data are in agreement with their early result, though the inclination drops before becoming larger.

4. Another modelization was done by Henderson ([1979](#)), in which the warp starts at 18.2 kpc (80′) with an increasing inclination in step of 0°.75 per kpc, and a warped region rotated by 10° with respect to the central disk position angle. This result is not totally consistent with our new result.

5. In the model of Brinks & Burton ([1984](#)), the disk starts to warp at ∼18 kpc, with a maximum warp angle of 15°. We detect a gradient of inclination in agreement with that value, though it is seen to occur at larger radius.

According to Brinks & Burton ([1984](#)), 39% of the total H I mass resides in the warped part of the disk. This number has to be compared with the gas mass of the main component integrated within $R > 27$ kpc ($0.14 \times 10^9 \, \mathcal{M}_\odot$) added to the total mass of all other spectral components than the main one ($1.74 \times 10^9 \, \mathcal{M}_\odot$). It corresponds to 44% of the total H I mass. This fraction is comparable with the prediction of Brinks & Burton ([1984](#)), though being slightly higher.

6. ORIGIN(S) OF THE OTHER SPECTRAL COMPONENTS

No kinematical analysis is presented for the other spectral components than the main disk component. Only a brief discussion on their possible origin(s) is proposed here. So many H I peaks like those observed in M31 are rarely evidenced in extragalactic sources. The sum of all of the integrated emission other than the main component represents 41% of the total H I mass. A significant fraction of it is due to the overlap emission from the warp whose signature is more prominent at large Y than along the major axis due to the inclination of the disk. Another part is due to an additional gas component whose origin(s) can be manifold.

A first origin could be structures lying in the disk itself, like, e.g., unresolved spiral arms by projection effects. Indeed, the 3rd, 4th, and 5th maps of Figure [6](#) show that projection effects may play an important role in creating multiple components due to the presence of more pixels at $|Y| > 0$ than along the major axis. Moreover, the projected spatial distribution of the gas in the multiple peaks is principally concentrated within high surface density regions, like the H I "ring" around 13 kpc and along the spiral arms. Note here that more components are detected in the northwestern front side of the galaxy than on the far side. Another internal origin of multiple components could be caused by expanding gas shells induced by stellar winds in star-forming regions. Such a phenomenon has already been seen in other galaxies (e.g., Hunter et al. [2001](#)). Several spectra of M31 show more or less symmetric peaks centered about the main component and could point out gas outflow in high-density regions of the M31 disk.

Other origins could be extraplanar gas in the form of, e.g., a lagging halo or high-velocity clouds. In recent deep H I observations a lagging halo corresponds to the thick gaseous layer that is observed to rotate more slowly than the host equatorial thin H I disk of spiral galaxies (Fraternali et al. [2001](#), [2002](#); Barbieri et al. [2005](#); Oosterloo et al. [2007](#)). The halo emission which is often referred to as an "anomalous" emission has a mass that can reach ∼30% of the total gas mass (Oosterloo et al. [2007](#)). It is thought to be gas infalling onto the disk, mainly due to a galactic fountain mechanism but also to the accretion from the intergalactic medium (Fraternali & Binney [2006](#), [2008](#)). Models of gas in the halo show it has a larger velocity dispersion than gas in the cold disk (Oosterloo et al. [2007](#)). The DRAO datacube exhibits many H I peaks whose

radial velocity is observed to be closer to the systemic velocity than the main H I disk component and whose velocity dispersion is larger than the main disk component. It implies that M31 could host a lagging halo as well.

High or intermediate velocity clouds (HIVC) similar to those orbiting around the MW (Wakker et al. [1999](#)) are observed in a few galaxies among which M31 is a very good candidate (Thilker et al. [2004](#); Westmeier et al. [2005](#)). M31 HIVCs detected by Westmeier et al. ([2005](#)) have a typical mass $\propto 10^5 \, \mathcal{M}_\odot$ for a size of ∼ 1 kpc. Similar HIVCs could be detected in the DRAO field of view. Indeed the minimum detectable column density of the data corresponds to $1.6 \times 10^4 \, \mathcal{M}_\odot$ per spatial resolution element (synthesized beam size).

One finally notices that no obvious forbidden velocities are detected in the high-resolution datacube of M31 at a 3σ detection level. Forbidden velocity clouds (FVC) correspond to apparent counterrotating gas, like in NGC 2403, NGC 891, or NGC 6946 (Fraternali et al. [2002](#); Oosterloo et al. [2007](#); Boomsma et al. [2008](#)). The presence of FVC could point out ongoing accretion onto a host disk. As a consequence if any H I gas accretion responsible for part of the multiple lines is occurring in M31, it does not seem to be done from apparent counterrotating material. A more careful search of HIVC or FVC in our datacube will require to filter the high-resolution datacube in the spatial and spectral dimensions to increase the signal-to-noise ratio.

7. THE H I OUTSKIRTS

7.1. The NE and SW Spurs

Neutral gas in M31 is detected out to ∼34.1 kpc in projection (∼36.3 kpc) in the SW approaching side (NE receding side, respectively). Two extended thin spurs are observed at the northeastern extremity of the disk while gas seems more confined in its southwestern extremity. These structures are connected to the spiral arms as seen in Figures [4](#), [5](#), and [12](#).

A column density of 6.2×10^{20} cm^{-2} is reached in the southwestern H I extension. A velocity gradient is detected from -515 km s^{-1} to -530 km s^{-1} for a length of ∼30′ (6.8 kpc), in apparent continuity of the disk kinematics. The velocity dispersion of the H I peaks is 12 km s^{-1} in its northern part while and lower values are seen in its southern part.

The NE spur (N1) is oriented north–south and has a length of ∼40′ (9.1 kpc). Its kinematics is in continuity with that of the disk. A velocity gradient from -85 km s^{-1} to -65 km s^{-1} is detected along it while the velocity dispersion of the H I lines remains constant (∼8–10 km s^{-1}). The highest H I density column observed in it is 4.8×10^{20} cm^{-2}. A small "hook-like" structure at $\alpha_{2000} = 00^{\rm h}49^{\rm m}11\overset{\rm s}{.}86, \delta_{2000} = +43^{\rm d}06'24''$ is observed as part of the spur. The other spur-like structure (N2) is shorter (∼30′). A velocity gradient is also observed along it, from -160 km s^{-1} to -140 km s^{-1}. Its velocity dispersion is very low (∼5 km s^{-1}) and is also seen to be constant. An average column density of 6×10^{19} cm^{-2} is derived for it. Note that the three H I extensions have very few pixels with multiple spectral components.

Are these structures real? What could be their origin(s)? One has to notice first that these extensions are genuine structures of the disk because they are also observed in the WSRT image (Braun et al. [2009](#)) and they cannot be mistaken with residuals from a bad subtraction of MW H I due to their kinematics. Then the kinematical properties of the two NE spurs strongly differ from each other. We argue that they are part of two different
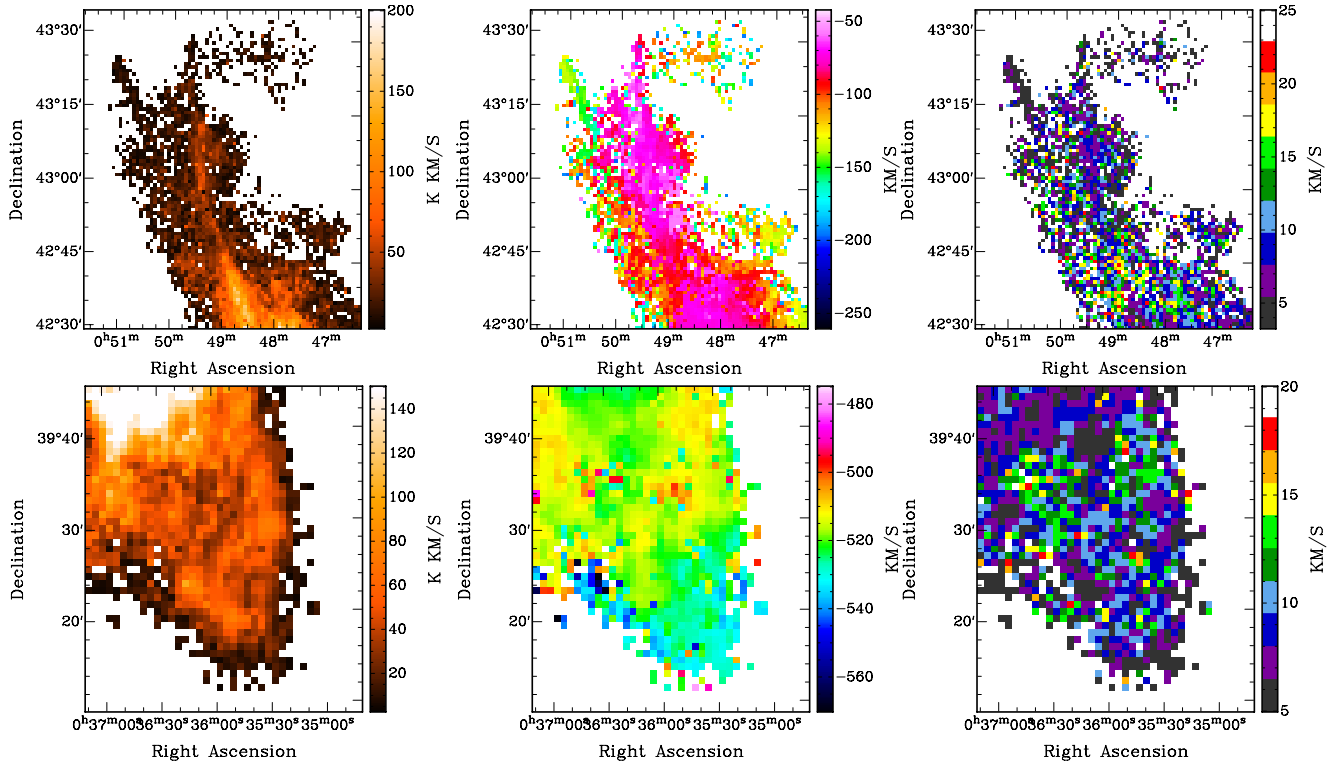
Figure 12. H I emission, velocity and velocity dispersion maps zoomed in the region of the NE (top panel) and SW (bottom) structures.
(A color version of this figure is available in the online journal.)

H I structures, though they are located in the same area of the field of view. On one hand a close inspection of the datacube points out that the spur N2 seems to be a kinematical extension of the external spiral arm of M31 (Figure 5). On another hand the brightness and kinematical properties of the spur N1 and the SW extension are quite similar. In particular they are responsible for the velocity rise that occurs at the outermost radii of the rotation curve. What is also remarkable with them is that they both overlay or point toward two diffuse stellar clumps, as seen in Figure 13. This image displays the H I column density contours superimposed onto the stellar distribution, as measured from deep photometry (Ibata et al. 2001, 2005, 2007). The SW extension is coincident with the G1 clump while the NE spur coincides with part of the northeast clump. According to Ibata et al. (2005) stars in the G1 clump rotates by 68 km s^{-1} faster than the disk, which is considered to rotate at $\sim$230 km s^{-1} in their model. The true rotation velocity in the southwestern extension is not observed constant at large radii, but increasing. This increase implies a lagging velocity of up to 45 km s^{-1} larger than the velocity of $\sim$230 km s^{-1}. The lagging velocity of gas is thus lower than that of stars. The spur N1 to the northeast is observed to rotate faster than $v_{\rm rot} = 230$ km s^{-1} as well by a similar amplitude than in the southern spur, while the NE stellar clump is observed to rotate slower. Hence gas and stars follow the same velocity trend in the SW region of the disk, while it does not seem to be the case in the NE region. Note however that stellar velocities are less certain in the NE clump because of the contamination by MW stars. It nevertheless indicates a strong relationship between stars and gas at the outskirts of M31, at least in the SW region.

The star formation history and metallicities of the northeast and G1 overdensities led Faria et al. (2007) and Richardson et al. (2008) to propose that they could be material initially formed into the disk that have been stripped by tidal effects. The
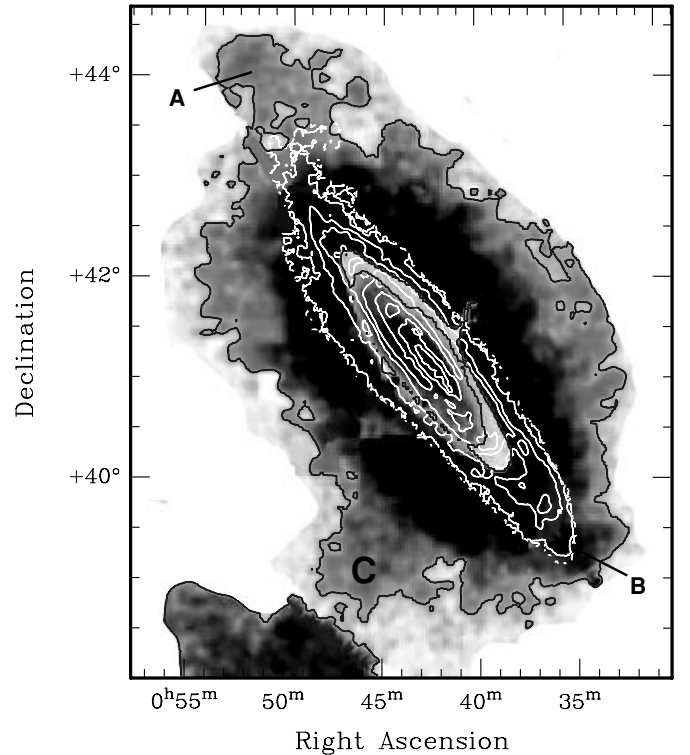
Figure 13. Comparison of the H I distribution (white contours) with the faint extended stellar disk of M31 from Ibata et al. (2007, gray-scale image and gray contours adapted from their Figure 50.). The letter A refers to the northeast stellar clump, B to the G1 clump, and C to the Giant Stream, following the nomenclature of Ibata et al. (2007). H I contours are for column densities of 5×10^{19}, 1×10^{20}, 4×10^{20}, 9×10^{20}, and 2×10^{21} cm^{-2}.

kinematics of the H I spurs imply that they are bound to the disk. Though they seem to rotate faster than gas, it is likely that stars in
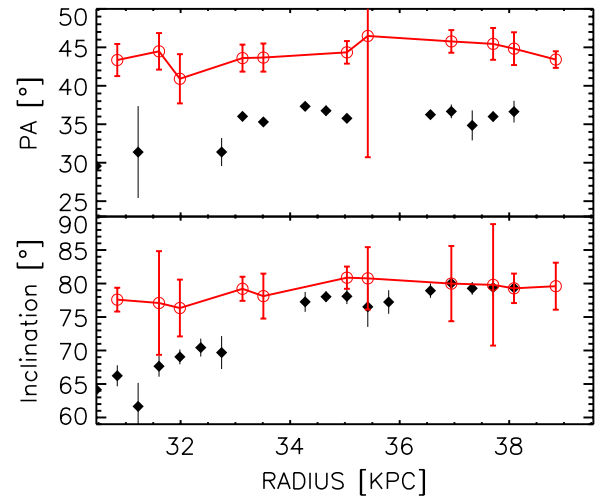
the external clumps are also bound to the disk of M31. A fit to the velocity field of a radial motion $v_{rad} \sin(i) \sin(\theta)$ in addition to the rotational one gives an average value $\bar{v}_{rad} = 6.2$ km s^{-1} with a standard deviation of 7.4 km s^{-1} for $R > 150'$ ($R > 35$ kpc).

By assuming that the spiral arms are trailing in the disk and by looking at the distribution of dust lanes in optical images of M31, the front side of the galaxy is to the NW of the major axis and the rotation is done counterclockwise. Therefore, at first order outflow motions are detected in the outskirts of M31 because of the derived positive radial velocities. At second order these radial motions could be mistaken by the presence of either vertical motions to the galaxy plane, which would thus be of the order of 35 km s^{-1} for the observed inclination ($80°$, Figure 9), or elliptical streaming in, e.g., a $m = 2$ perturbing potential. However, that latter hypothesis is less uncertain here because no evident spiral structure is seen at those radii but rather thin "filamentary" H I spurs. The reality is probably a combination of these hypotheses (pure outflow, z-motions, and elliptical streaming). $\bar{v}_{rad} \sim 6$ km s^{-1} is likely an upper limit of any possible outflowing motions. Such radial motions are consistent with the scenario proposed by Faria et al. (2007) or Richardson et al. (2008). Indeed, one expect outflow motions in the disk outskirts if tidal stripping is occurring. N-body models would be helpful to firmly validate the detection of ongoing outflow in the outskirts of M31.

7.2. The External Arm

The external arm is another new perturbed structure in M31. It has many properties different from other disk structures. It has no identifiable morphological and kinematical symmetric counterpart[5] with respect to the galactic center. Its kinematics significantly differs from radial velocities within the disk (Figure 5). It does not contain so many pixels with multiple H I peaks. It is one of the faintest structures detected in the field of view with a brightness comparable to interarm regions. The total H I mass attached to this structure is $1.1 \times 10^8 \, \mathcal{M}_\odot$. Its apparent length is $2°.33$ or 32 kpc. The kinematical difference with the disk is caused by different orientation angles. Indeed its position angle and inclination are $\sim 10°$ larger than those of the disk (Figure 14), with the exception of the region $R > 34$ kpc where both inclinations become very similar. The rotation velocities of the external arm are comparable with the disk rotation curve. No obvious stellar counterpart to the gaseous arm can be identified in the optical images of Ibata et al. (2005, 2007) because of their too high contrast.

Here again one may question about its origin. Internally driven perturbations are hardly possible because one would expect the creation of axisymmetric or bisymmetric features in the gas distribution (e.g., a bar, a ring, or two spiral arms). The apparent isolated nature of the arm on one half of the disk and not on the other side rules out this hypothesis and points out to an external perturbation for its origin. It includes spiral arm triggering by tidal effects exerted by a companion or even gas accreted from a companion. This would be more consistent given the perturbed nature of the stellar distribution at large radius caused by tidal interactions with low-mass satellites. Indeed the stellar halo of M31 is filled of stellar residuals from past interactions with smaller galaxies. M31 has currently two nearby bright satellites, M32 and NGC 205 at projected

---

[5] The only noteworthy H I feature which could be a counterpart on the other edge of the disk is located around $\alpha_{2000} = 00^h39^m49°.80$, $\delta_{2000} = +41°13'39''$. However, it is not an extended structure like the external arm.

Figure 14. H I inclination and position angle of the external arm (open symbols). The filled symbols show the orientation of the disk parameters from Figure 9.

(A color version of this figure is available in the online journal.)

distances of ~ 25 kpc and ~ 37 kpc to the M31 nucleus. Both are expected to have interacted with M31. In a gas accretion scenario, one would need an efficient tidal stripping because both companions are devoid of gas. Block et al. (2006) simulated a head-on collision with M32 that could have occurred 210 million years ago and have generated the ring-like morphology in the distribution of dust and gas. Howley et al. (2008) simulated an interaction with NGC 205 and found radial orbits at high velocity (up to 500 km s^{-1}) for the small companion. According to the possible orbits from the models, we think the most likely impactor that generated the external arm could be NGC 205. The location of the perturbed external arm indeed coincides with the path of NGC 205 in the apparent far side of the galaxy (see Figure 19 of Howley et al. 2008) while the M32 trajectory leads the compact elliptical close to the M31 center along a polar orbit. Here again more detailed numerical simulations are needed to investigate the different possibilities and find the origin of this perturbation.

8. MASS DISTRIBUTION ANALYSIS

The mass distribution modeling of the galaxy is done by decomposing the total gravitational potential into a supermassive black hole, a luminous baryonic component and a dark matter component. It consists in fitting a dynamical model for the dark matter component to the observed rotation curve, taking into account the baryonic rotation curves. Two or three free parameters are fitted for the halo in addition to the stellar mass-to-light ratios for the bulge and galactic disk. These latter can be fixed under some assumptions described below.

8.1. The Central Supermassive Black Hole

Messier 31 is known to have a central supermassive black hole which mass can now be robustly constrained. The black hole contribution to the rotation curve remains negligible through the disk because of the point mass nature of its gravitational potential. A mass of $1.4 \times 10^8 \, \mathcal{M}_\odot$ was derived using *Hubble Space Telescope* STIS spectroscopy of the nucleus (Bender et al. 2005) and is used in our study.

8.2. The Luminous Baryonic Matter

The contribution of the luminous baryons to the rotation curve consists in stellar and gaseous components.

8.2.1. The Stellar Potential

The gravitational potential of the stars is decomposed into contributions from a bulge and a disk. These ones are derived from the R-band surface brightness profile of M31 (Walterbos & Kennicutt 1987, 1988).

A bulge–disk decomposition of the surface brightness profile is done using an exponential disk contribution for the stellar disk plus a de Vaucouleurs $R^{1/4}$ law (de Vaucouleurs 1948) for the bulge contribution. However, the de Vaucouleurs law gives a bad result for the bulge contribution to the surface brightness profile because it significantly overestimates the intensity in the inner parts of the galaxy. A more robust bulge–disk decomposition is done using a generalized Sérsic $R^{1/n}$ model for the bulge light (Sérsic 1963, 1968) plus an exponential disk. In the Sérsic model, the intensity profile is written as

$$I(R) = I_e \exp\{-b_n[(R/R_e)^{1/n} - 1]\}, \qquad (1)$$

in which I_e is the intensity at the effective radius R_e defined as the radius that contains half of the total light and n is a dimensionless index that measures the "curvature" of the luminosity profile. b_n is a function of n and is defined as $b_n = 1.9992n - 0.3271$ for $0.5 < n < 10$ (Capaccioli 1989). The de Vaucouleurs law is thus a specific case of the Sérsic law for $n = 4$.

The stellar disk intensity profile is fitted with the exponential disk formula (see, e.g., Freeman 1970)

$$I(R) = I_0 \exp(-R/R_d), \qquad (2)$$

where I_0 is the intensity at $R = 0$ and R_d the scale-length of the disk.

The two components were fitted simultaneously to the brightness profile (Figure 15). The fitted bulge parameters are $R_e = (1.3 \pm 0.1)$ kpc, $\mu_e = (18.6 \pm 0.1)$ mag arcsec^{-2} (not corrected for foreground and internal dust attenuation), and $n = 1.1 \pm 0.1$. The total apparent magnitude of a bulge for the Sérsic law is given by

$$m = \mu_e - 5 \log R_e - 2.5 \log \left[2\pi n \frac{e^{b_n}}{(b_n)^{2n}} \Gamma(2n) \right] \qquad (3)$$

(Graham & Driver 2005), which gives a total uncorrected apparent magnitude of $m_{\mathrm{Bulge}} \sim 3.25$ mag for M31.

The fitted disk parameters are $R_d = (5.6 \pm 0.1)$ kpc and a central surface brightness $\mu_0 = (19.0 \pm 0.1)$ mag arcsec^{-2} (not corrected for foreground and internal dust attenuation nor inclination effects). This disk scale-length compares well with values fitted with the same dataset (Walterbos & Kennicutt 1987, 1988; Geehan et al. 2006). As seen in Figure 15, the adopted disk brightness profile is nevertheless not the fitted one, but the result of the subtraction of the fitted bulge contribution to the observed profile. This allows us to keep the stellar surface brightness as close as possible to the observed profile. Moreover, it enables us to keep the intensity variations of the disk that could reproduce wiggles in the rotation curve. The surface brightness profiles are then corrected from Galactic extinction (following Schlegel et al. 1998) and for inclination effects (only for the disk profile) and for internal extinction as described in Section 8.2.2.
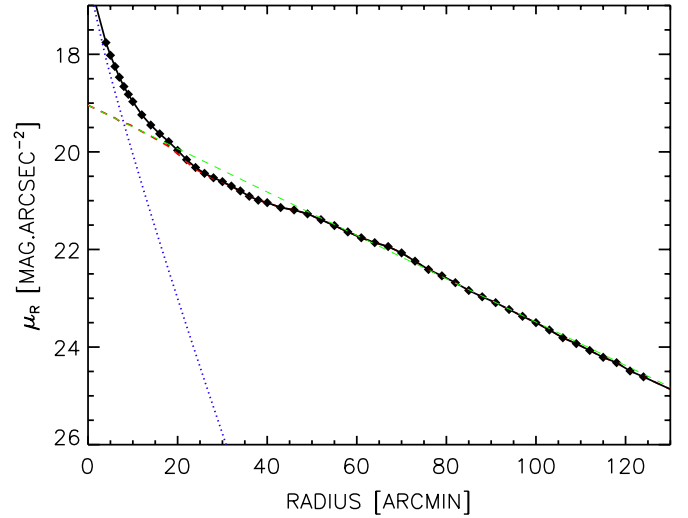
Figure 15. R-band surface brightness profile of Messier 31. Observations are from Walterbos & Kennicutt (1987). The filled symbols are the observations, a red dashed line is the adopted contribution of the disk to the surface brightness, a blue dotted line the adopted contribution of the bulge, and a solid line the sum of both components. A green dashed line shows the fit of the exponential disk.

(A color version of this figure is available in the online journal.)

8.2.2. The Mass-to-Light Ratios of the Stellar Component

Two free parameters of the mass models are the mass-to-light ratios of the bulge $\Upsilon_{\mathrm{Bulge}}$ and of the galactic disk Υ_{Disk}, which are considered constant as a function of radius for the remainder. Models presented here also enable these parameters to be fixed. A relative approximation for them can be deduced from stellar population synthesis (SSP) models (e.g., Bell et al. 2003), provided that a color is given.

The bulge color is $B - R = 1.75$ mag (Walterbos & Kennicutt 1988), which gives a color of $B - R \sim 1.27$ after correction for foreground and internal dust extinction effects. Here we have applied the reddening law for M31 derived by Barmby et al. (2000), using a mean reddening factor $E_{B-V} = 0.24$ mag (Williams & Hodge 2001). This reddening law is relatively comparable with the one measured for the MW. The corrected bulge mass-to-light ratio is $\Upsilon_{\mathrm{Bulge}} \sim 2.2 \, \mathcal{M}_\odot/L_\odot$, following the prescriptions of Bell et al. (2003). These authors indicate a rms scatter of the order of 25% on the mass-to-light ratios. An independent constraint of the bulge mass-to-light ratio can be obtained directly from measurements of the bulge effective stellar velocity dispersion, with the assumption that the dark halo has a negligible contribution to the velocity dispersion. The estimated dynamical mass of the bulge is $\mathcal{M}_{\mathrm{Bulge}} = 1.9 \times 10^{10} \, \mathcal{M}_\odot$ (Marconi & Hunt 2003), which value becomes $\mathcal{M}_{\mathrm{Bulge}} = 2.4 \times 10^{10} \, \mathcal{M}_\odot$ after scaling to our adopted bulge effective radius. It implies a corrected dynamical mass-to-light ratio of $\Upsilon_{\mathrm{Bulge}} \sim 0.8 \, \mathcal{M}_\odot/L_\odot$. This is about 2.8 times lower than the ratio derived from SSP models.

The average disk color is $B - R \sim 1.6$ mag, as derived from Walterbos & Kennicutt (1987), giving a corrected color $B - R \sim 1.1$ mag and a corrected disk mass-to-light ratio $\Upsilon_{\mathrm{Disk}} \sim 1.7 \, \mathcal{M}_\odot/L_\odot$. When no correction from internal extinction is applied to the $B - R$ colors, SSP models imply $\Upsilon_{\mathrm{Bulge}} \sim 4.0$ and $\Upsilon_{\mathrm{Disk}} \sim 3.2$. Our values of corrected and uncorrected Υ_{Disk} are thus in good agreement with those estimated by Widrow & Dubinski (2005) or Geehan et al. (2006).

Applying the same foreground and internal corrections as above (using $A_B = 0.67$ mag, de Vaucouleurs et al. 1991), the

total bulge luminosity of M31 is $L_{\rm Bulge} \sim 2.9 \times 10^{10}\ L_\odot$ in the R-band, which translates into a total corrected bulge mass of $\mathcal{M}_{\rm Bulge} \sim 6.4 \times 10^{10}\ \mathcal{M}_\odot$ for the adopted $\Upsilon_{\rm Bulge} = 2.2$. The deduced total luminosity of the disk (also corrected for inclination) is $L_{\rm Disk} \sim 4.2 \times 10^{10}\ L_\odot$, corresponding to a total corrected stellar disk mass of $\mathcal{M}_{\rm Disk} \sim 7.1 \times 10^{10}\ \mathcal{M}_\odot$ for the adopted $\Upsilon_{\rm Disk} = 1.7$. The total inferred stellar mass is $\mathcal{M}_\star \sim 1.35 \times 10^{11}\ \mathcal{M}_\odot$. SSP models thus infer disk and bulge masses comparable with each other, which is somewhat unexpected for a high surface brightness galaxy (Courteau & Rix 1999). If one uses the dynamical value $\Upsilon_{\rm Bulge} = 0.8$ instead of the SSP value, then the total stellar mass becomes $\mathcal{M}_\star \sim 9.5 \times 10^{10}\ \mathcal{M}_\odot$, making the bulge-to-disk mass ratio falling down to 34%, which seems more realistic.

8.2.3. Infrared Surface Photometry

Determining mass-to-light ratios for galaxies in the 3.6 μm band from stellar synthesis models is not an easy task because no straightforward recipe exists at this wavelength, contrary to optical bands.

We have attempted to derive stellar mass-to-light ratios and masses from observations performed with the *Spitzer*-IRAC at 3.6 μm (Barmby et al. 2006). However, no realistic stellar masses and mass-to-light ratios could be estimated, using either the formalism developed in de Blok et al. (2008) that derives mass-to-light ratios from the Large Galaxy Atlas of the Two Micron All Sky Survey (2MASS) $J - K$ bulge and disk colors, or the average values of bulge and disk mass-to-light ratios inferred for seven barred and unbarred Sab, Sb, and Sbc spirals from the THINGS galaxy sample of de Blok et al. (2008). Such values both lead to either a too large total stellar mass or a too massive bulge compared with the disk. As a consequence mass distribution models have been fitted using the only R-band photometry for clarity and simplicity reasons.

8.2.4. The Gaseous Disk Potential

The contribution to the rotation curve from the gaseous component is derived from the H$_2$ and H I surface densities. The H$_2$ surface density is taken from the CO gas survey of Dame et al. (1993), after scaling to our adopted distance. The total molecular mass is $\sim 3.5 \times 10^8\ \mathcal{M}_\odot$. The H I surface density profile is determined by averaging the total H I emission over elliptical rings which orientations are given by the tilted-ring model described in Section 5.1.

The H I surface density profile is displayed in Figure 16, for the total H I distribution and for the principal emission component (the one that served to build the velocity field). The profile of the total H I distribution is listed in Table 4. It has been derived using orientation parameters of Figure 9 and Table 4. No correction due to the overlap from the warp emission has been applied to the density profile because no three-dimensional model of the datacube has been attempted in this paper. It has no consequences on the following result because of the very low induced amplitudes of the atomic gas rotation velocities.

The majority of H I gas is located between $R = 7$ kpc and $R = 18$ kpc, which corresponds to the location of the brightest "rings." Peaks are also observed in the inner region, in agreement with the locations of other inner ring-like structures. The rotation curve of the atomic gas component is then derived after scaling the density profile by a factor of ~ 1.3 in order to take into account the helium contribution. The contribution of the atomic gas to the overall rotation curve is very low and does not exceed ~ 70 km s^{-1}. As the mass of the molecular gas is only $\sim 8\%$ that
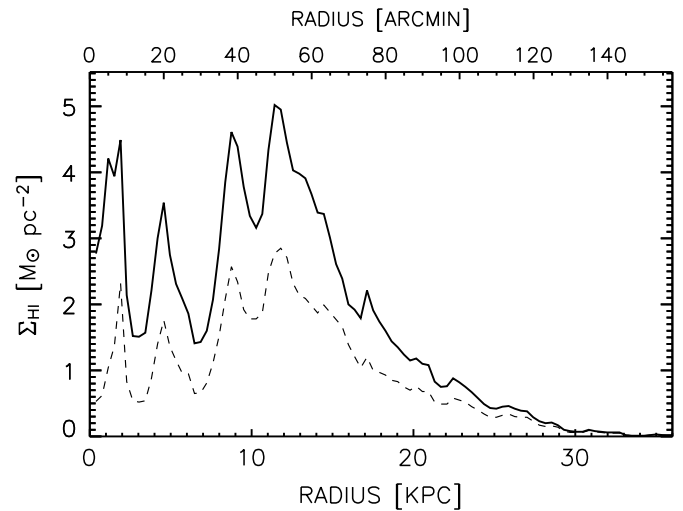
Figure 16. H I surface density profile of Messier 31. A full line is for the total H I emission, a dashed line for the emission of the main component.

of the total atomic gas, its contribution to the rotation curve is also very low (~ 15 km s^{-1} at maximum) and comparable with the velocities due to the black hole at the largest distances. The mass-to-light ratios of the molecular and atomic components are kept fixed during the fittings ($\Upsilon_{\rm gas} = 1$).

8.3. The Dark Matter Halo Potential

Three different halos are fitted in this study. A first model is associated with a pseudo-isothermal sphere while two other models are cosmological halos as their density profile is derived from CDM numerical simulations. No attempts to fit the mass distribution in triaxial models were done as all models consider a spherical halo. Also, no attempt to model an adiabatic contraction of the dark halo in its central parts was done (Dutton et al. 2005).

8.3.1. Navarro–Frenk–White Halo

Navarro et al. (1996, 1997) were among the first ones to propose a formalism that was fitted to results from numerical simulations done in the framework of the CDM theory. They found a halo shape that is independent of the halo mass, which is why this halo is often referred to as the "universal" halo. The mass density profile is steep (cuspy) as it scales with R^{-1} at low radius and is written as

$$\rho_{\rm nfw}(R) = \frac{\delta_c\ \rho_{\rm crit}}{(R/R_s)(1 + (R/R_s)^2)}, \qquad (4)$$

where $\rho_{\rm crit} = 3H_0^2/(8\pi G)$ is the critical density for closure of the universe, δ_c represents a characteristic density contrast and R_s a scale radius. The circular velocity profile corresponding to this halo allows to fit two parameters, V_{200}, the velocity at the virial radius R_{200}, and $c = R_{200}/R_s$, a concentration parameter of the halo, to the observed rotation curve, and is written as

$$V(R) = V_{200}\sqrt{\frac{1}{x}\frac{\ln(1+cx) - cx/(1+cx)}{\ln(1+c) - c/(1+c)}}. \qquad (5)$$

In this equation, $x = R/R_{200}$. This model is referred to as the "NFW" model or NFW halo hereafter.

Table 4
H I Rotation Curve, Surface Density, Disk Inclination, and Position Angle from Tilted-ring Model Results

Radius (′)	Radius (kpc)	P.A. (°)	$e_{P.A.}$ (°)	P.A.$_{adopted}$ (°)	i (°)	e_i (°)	$i_{adopted}$ (°)	v_{rot} (km s^{-1})	$e_{v_{rot}}$ (km s^{-1})	Σ_{HI} ($\mathcal{M}_\odot$ pc^{-2})
1.67	0.38	...	...	26.6	...	...	31.0	...	...	2.77
3.33	0.76	...	...	26.6	...	...	31.0	...	...	3.19
5.00	1.14	...	...	26.6	...	...	31.0	336.2	171.7	4.21
6.67	1.52	...	...	26.6	...	...	31.0	324.6	125.1	3.94
8.33	1.90	26.6	2.5	26.8	30.5	4.3	31.0	339.0	52.8	4.49
10.00	2.28	27.1	2.2	27.3	62.4	4.3	51.0	243.6	25.8	2.14
11.67	2.66	27.7	1.9	28.6	61.0	3.4	61.3	235.2	17.0	1.52
13.33	3.04	30.7	1.5	30.6	66.3	2.7	65.8	238.9	5.7	1.51
15.00	3.43	33.5	1.3	32.2	70.4	3.0	68.1	239.3	18.3	1.57
16.67	3.81	32.6	1.2	32.7	...	...	67.7	226.3	16.1	2.21
18.33	4.19	32.3	1.0	32.9	69.3	1.5	67.3	202.6	4.7	3.00
20.00	4.57	...	...	33.3	62.5	1.0	64.4	207.3	10.7	3.54
21.67	4.95	...	...	33.6	60.8	1.2	63.7	202.5	21.7	2.75
23.33	5.33	33.4	0.9	33.9	66.8	1.3	65.9	208.9	15.6	2.31
25.00	5.71	36.0	0.5	35.4	69.7	1.4	68.1	221.6	13.4	2.09
26.67	6.09	37.0	0.6	36.4	66.8	0.7	69.7	232.2	13.7	1.86
28.33	6.47	36.3	0.5	36.6	74.3	0.8	72.0	237.6	8.3	1.41
30.00	6.85	36.9	0.4	36.5	73.2	0.4	73.5	239.8	2.2	1.43
31.67	7.23	35.7	0.3	36.4	74.6	0.6	74.3	235.6	6.1	1.60
33.33	7.61	37.0	0.2	36.8	75.0	0.4	74.6	241.7	3.3	2.07
35.00	7.99	37.2	0.2	37.3	74.6	0.4	74.5	244.3	6.4	2.84
36.67	8.37	37.9	0.2	37.7	73.7	0.4	74.3	248.8	6.4	3.85
38.33	8.75	38.1	0.3	38.0	74.8	0.4	74.3	251.8	5.5	4.61
40.00	9.13	38.0	0.3	38.3	73.8	0.5	74.4	253.0	9.2	4.39
41.67	9.51	38.9	0.2	38.7	75.0	0.5	74.8	258.8	9.6	3.78
43.33	9.90	39.1	0.2	39.0	75.2	0.4	75.2	259.0	9.5	3.34
45.00	10.28	39.2	0.2	39.1	75.3	0.4	75.6	262.2	10.8	3.16
46.67	10.66	39.1	0.2	39.0	76.7	0.4	76.1	266.8	13.0	3.37
48.33	11.04	38.7	0.2	38.8	76.1	0.3	76.3	266.8	11.7	4.34
50.00	11.42	38.5	0.2	38.6	76.6	0.3	76.4	265.9	9.9	5.02
51.67	11.80	38.7	0.2	38.3	76.5	0.3	76.3	264.4	7.2	4.95
53.33	12.18	37.8	0.2	37.7	76.1	0.3	76.0	264.7	5.3	4.45
55.00	12.56	36.8	0.2	37.0	75.5	0.3	75.6	265.3	5.4	4.03
56.67	12.94	36.1	0.2	36.4	75.1	0.3	75.1	265.2	3.9	3.98
58.33	13.32	36.3	0.2	36.1	74.7	0.3	74.8	262.0	2.4	3.91
60.00	13.70	35.5	0.2	35.9	74.7	0.3	74.5	260.8	4.5	3.67
61.67	14.08	36.0	0.2	36.1	73.9	0.4	74.3	259.2	5.4	3.39
63.33	14.46	36.6	0.2	36.6	74.9	0.3	74.1	258.1	6.8	3.37
65.00	14.84	37.3	0.2	37.1	72.9	0.3	73.7	258.4	6.1	3.01
66.67	15.23	37.3	0.2	37.3	73.7	0.3	73.7	259.2	4.6	2.61
68.33	15.61	37.4	0.2	37.2	73.9	0.3	74.1	262.7	4.2	2.39
70.00	15.99	36.8	0.2	37.1	74.5	0.3	74.7	266.1	4.0	2.00
71.67	16.37	37.2	0.2	37.3	75.8	0.3	75.4	270.0	2.3	1.92
73.33	16.75	37.9	0.2	37.7	75.7	0.3	75.5	269.8	1.0	1.79
75.00	17.13	38.1	0.2	37.7	75.6	0.3	75.1	269.1	3.9	2.21
76.67	17.51	37.1	0.2	37.5	73.7	0.4	74.3	268.5	7.1	1.91
78.33	17.89	37.5	0.2	37.5	74.2	0.5	73.8	263.0	15.0	1.74
80.00	18.27	37.7	0.3	37.5	72.8	0.5	73.4	257.1	13.5	1.60
81.67	18.65	37.1	0.3	37.4	73.4	0.5	73.4	254.1	10.6	1.44
83.33	19.03	...	...	37.5	73.8	0.5	73.6	251.9	11.1	1.35
85.00	19.41	37.1	0.3	37.7	73.7	0.5	73.4	249.5	8.1	1.24
86.67	19.79	38.8	0.3	38.3	...	...	73.2	245.7	7.4	1.15
88.33	20.18	39.2	0.3	38.6	72.5	0.6	73.0	243.7	6.6	1.18
90.00	20.56	37.9	0.3	38.3	...	...	73.0	245.9	7.5	1.10
91.67	20.94	37.7	0.3	38.2	...	...	73.0	242.3	6.1	1.08
93.33	21.32	38.9	0.3	38.4	73.0	0.5	73.0	239.2	6.3	0.83
95.00	21.70	38.3	0.3	38.2	73.0	0.6	73.3	239.5	4.7	0.75
96.67	22.08	37.5	0.3	37.8	74.3	0.6	73.5	236.1	1.8	0.76
98.33	22.46	37.4	0.3	37.5	72.9	0.4	73.4	233.8	1.7	0.88
100.00	22.84	37.5	0.3	37.6	73.3	0.5	73.3	233.1	3.3	0.82
101.67	23.22	38.0	0.3	37.7	73.6	0.5	73.3	230.1	5.5	0.75
103.33	23.60	37.4	0.3	37.7	72.9	0.5	73.2	232.1	5.0	0.67
105.00	23.98	37.6	0.3	37.7	73.4	0.6	73.2	228.7	1.7	0.58
106.67	24.36	...	...	37.8	73.0	0.6	73.2	229.1	1.8	0.49
108.33	24.75	38.0	0.3	38.0	73.5	0.6	73.4	227.9	5.0	0.43

Table 4
(Continued)

Radius (′)	Radius (kpc)	P.A. (°)	$e_{P.A.}$ (°)	P.A.$_{adopted}$ (°)	i (°)	e_i (°)	$i_{adopted}$ (°)	v_{rot} (km s^{-1})	$e_{v_{rot}}$ (km s^{-1})	Σ_{HI} ($\mathcal{M}_\odot$ pc^{-2})
110.00	25.13	...	...	38.0	73.8	0.6	73.6	226.9	2.0	0.42
111.67	25.51	38.5	0.3	38.1	...	...	73.6	225.1	1.6	0.45
113.33	25.89	37.6	0.3	38.1	...	...	73.7	225.4	1.8	0.46
115.00	26.27	38.4	0.3	38.3	73.1	0.5	73.7	230.3	2.0	0.42
116.67	26.65	...	...	38.4	74.5	0.5	74.0	229.0	2.3	0.39
118.33	27.03	38.9	0.3	38.5	74.2	0.5	73.9	229.9	4.8	0.38
120.00	27.41	38.0	0.3	38.4	73.3	0.7	73.5	230.1	6.6	0.29
121.67	27.79	38.5	0.3	38.2	72.4	0.9	73.6	229.8	3.0	0.23
123.33	28.17	37.8	0.3	37.8	75.6	0.5	74.0	230.4	5.2	0.20
125.00	28.56	37.2	0.3	37.4	73.7	0.9	73.5	230.9	2.9	0.21
126.67	28.94	37.0	0.3	37.0	71.5	1.1	72.5	229.8	2.1	0.17
128.33	29.32	36.6	0.5	36.4	73.3	1.5	71.3	228.8	1.8	0.10
130.00	29.70	36.2	0.4	34.9	68.2	2.0	69.3	238.3	3.3	0.08
131.67	30.08	31.7	1.3	32.5	67.8	1.8	67.2	243.6	1.4	0.07
133.33	30.46	29.6	1.7	31.0	64.2	2.5	65.7	247.3	3.1	0.07
135.00	30.84	...	...	31.1	66.2	1.6	64.8	247.8	1.3	0.10
136.67	31.22	31.4	6.0	31.3	61.7	3.5	64.8	248.4	2.0	0.08
138.33	31.61	...	...	31.6	67.7	1.6	66.6	248.1	1.5	0.07
140.00	31.99	...	...	32.0	69.1	1.1	68.7	244.5	1.6	0.06
141.67	32.37	...	...	32.3	70.4	1.3	70.1	244.4	3.0	0.06
143.33	32.75	31.4	1.8	32.6	69.7	2.5	72.1	241.7	4.3	0.06
145.00	33.13	36.0	0.3	34.5	...	...	72.9	237.7	1.9	0.02
146.67	33.51	35.3	0.4	35.8	...	...	73.7	237.6	6.1	0.01
148.33	33.89	...	...	36.2			74.5	244.9	3.6	0.01
150.00	34.27	37.3	0.3	36.5	77.3	1.5	75.2	247.9	3.2	0.01
151.67	34.66	36.8	0.6	36.5	78.0	0.8	77.3	256.3	3.1	0.02
153.33	35.04	35.8	0.5	36.3	78.1	1.2	77.6	253.5	4.1	0.03
155.00	35.42	...	...	36.3	76.5	3.0	77.3	244.3	4.7	0.02
156.67	35.80	...	...	36.3	77.2	1.8	77.7	249.3	5.8	0.02
158.33	36.18	...	...	36.3			78.2	255.7	4.5	0.02
160.00	36.56	36.2	0.4	36.3	78.9	1.1	78.7	255.0	5.8	0.02
161.67	36.94	36.7	0.9	36.5	80.0	0.7	79.4	271.1	7.8	0.03
163.33	37.32	34.8	2.0	36.6	79.3	0.9	79.5	269.8	4.7	0.03
165.00	37.71	36.0	0.6	36.7	79.4	1.4	79.4	258.2	10.7	0.03
166.67	38.09	36.6	1.4	36.7	79.3	1.2	79.4	275.1	4.8	0.02

8.3.2. Einasto Halo

Merritt et al. (2005, 2006) used more recent ΛCDM numerical simulations to model the mass density profile of dark halos and found that they can be fitted with a three-parameter model. The density is written as

$$\rho_{ein}(R) = \rho_e \exp\{-d_n[(R/R_e)^{1/n} - 1]\}. \quad (6)$$

This relation is very similar to the expression of the luminosity profile for elliptical galaxies and bulges of galaxies (Equation (1)), with the difference that the Sérsic formula applies to the (projected) surface distribution of light from galaxies whereas Equation (6) applies to the spatial distribution of the halo mass. Like in Equation (1), n is a dimensionless parameter which measures the "curvature" of the density profile, d_n is a function of n and can be approximated by $d_n \approx 3n - 1/3 + 0.0079/n$ (Merritt et al. 2006), provided that $n \gtrsim 0.5$. Here, ρ_e is the density at the effective radius R_e defined as the radius of a sphere in which half of the total halo mass is contained.

The mass profile of the Einasto halo (Cardone et al. 2005; Mamon & Łokas 2005; Merritt et al. 2006) is written as

$$M_{ein}(R) = 4\pi n R_e^3 \rho_e e^{d_n} d_n^{-3n} \gamma(3n, x). \quad (7)$$

Here, $\gamma(3n, x)$ is the incomplete gamma function defined as

$$\gamma(3n, x) = \int_0^x e^{-t} t^{3n-1} dt. \quad (8)$$

Merritt et al. (2006) and Graham et al. (2006) refer to this model as the Einasto halo due to the early works made by Einasto (1965, 1968, 1969) and Einasto & Haud (1989) on the light and mass distributions of galaxies, independently from those of Sérsic (1968). Simulated empirical galaxy-sized halos have typical values $n = 5$–7 (Table 1 of Merritt et al. 2006), $\log(\rho_e) \sim -5.5$ ($\mathcal{M}_\odot$ pc^{-3}) and r_e of several hundreds of kpc. Hereafter, this model is referred to as model "EIN" or Einasto halo.

8.3.3. Core-dominated Halo

A halo having a volumic mass density which is constant at low radii is often referred to as a core-dominated halo or a (pseudo-) isothermal sphere. Several formalisms exist to describe such a halo shape (Blais-Ouellette et al. 2001, and references therein) and the following prescription is used:

$$\rho_{iso}(R) = \frac{\rho_0}{(1 + (R/R_c)^2)^{1.5}}, \quad (9)$$

Table 5
Mass Model Results Using the *R*-band Photometry

Halo Model	Parameter	SSP	HYB	BF
ISO	ρ_0	28.9 ± 4.9	83.1 ± 13.3	1.2 ± 0.1
	r_c	9.3 ± 0.8	6.0 ± 0.4	1347.3 ± 104481
	Υ_{Disk}	1.7	1.7	5.9 ± 0.3
	Υ_{Bulge}	2.2	0.8	1.0 ± 0.2
	χ_r^2	23.6	22.9	16.6
NFW	V_{200}	168.5 ± 9.2	146.2 ± 3.9	462.7 ± 52.6
	c	10.1 ± 1.4	20.1 ± 2.0	0.9 ± 0.1
	Υ_{Disk}	1.7	1.7	5.1 ± 0.3
	Υ_{Bulge}	2.2	0.8	1.1 ± 0.3
	χ_r^2	23.6	21.0	19.7
EIN	ρ_e	0.048 ± 0.196	0.001 ± 0.007	0.508 ± 1.083
	R_e	99.3 ± 174.5	426.0 ± 1222.7	34.9 ± 27.5
	n	3.5 ± 2.7	7.9 ± 5.2	4.0 ± 1.1
	Υ_{Disk}	1.7	1.7	0.001 ± 0.080
	Υ_{Bulge}	2.2	0.8	0.013 ± 0.857
	χ_r^2	23.8	20.7	21.2

Notes. Radii are in kpc, volumic mass densities in 10^{-3} $\mathcal{M}_\odot$ pc^{-3}, velocities in km s^{-1}, and mass-to-light ratios in $\mathcal{M}_\odot/L_\odot$. The reduced Chi-square χ_r^2 is given for each model.

where ρ_0 and R_c are the central mass density and the core radius of the halo. These are the parameters that are fitted to the rotation curve. This dark halo was used in Carignan et al. (2006). The volumic mass density decreases at large radius like $\rho \propto R^{-3}$, exactly as for the NFW halo. We refer to this halo as the "ISO model" and pseudo-isothermal or core halo.

8.4. Fittings

Levenberg–Marquardt least-squares fittings to the rotation curve of M31 are done. One model uses Υ_{Disk} and Υ_{Bulge} fixed at the SSP values of 1.7 and 2.2 (model referred to as "SSP"). Another hybrid model ("HYB") is fitted with $\Upsilon_{\text{Disk}} = 1.7$ and $\Upsilon_{\text{Bulge}} = 0.8$ (see Section 8.2.2).

We have also considered best-fit models ("BF") for both photometric bands, which have free halo and stellar parameters. Only one plot is shown for this model given that they lead to either very unconstrained parameters (e.g., the core radius), or too massive stellar disk (the so-called maximum disk fitting) or unphysical models (e.g., null mass-to-light ratios). This latter result is not acceptable for a high surface brightness galaxy like M31 and has to be rejected. Results of best-fit models are listed in Table 5 and are only used to provide a very upper limit of the total stellar mass of M31.

A usual normal weight is applied to the data points as the inverse of the square of the velocity uncertainties. Several tries are done with different sets of initial guesses in order to avoid as much as possible local minima. Furthermore, a constraint is applied to the mass densities which have to be positive in order to avoid hollow halos. Another final constraint is for the quantity n of the Einasto halo, which has to be larger than or equal to 0.5 because of the definition of d_n.

8.5. Results

Rotation curve decompositions are displayed in Figure 17 and fitted parameters listed in Table 5.

The basic results can be summarized as follows.

1. The reduced χ_r^2 are high, it is impossible to reproduce the exact perturbed shape of the rotation curve.

2. The rotation velocities in the nucleus are not reproduced. It is expected since this region has a very negligible weight in all fittings because of the large observed uncertainties.
3. All models with a fixed $\Upsilon_{\text{Bulge}} = 2.2$ significantly overestimate the dip at 4 kpc, sometimes with a velocity difference of up to 60 km s^{-1}, as seen in the top-left panel of Figure 17.
4. Hybrid models with a fixed $\Upsilon_{\text{Bulge}} = 0.8$ gives better results than pure SSP models.
5. For each of the HYB and SSP model, the quality of the fit is equivalent whatever the shape of the dark matter halos is.

8.6. Analysis

High χ_r^2 values are in majority caused by the peculiar shape of the high-resolution rotation curve, which is hard to reproduce irrespective of the halos and mass-to-light ratios used during the fittings. From a statistical point of view, the derived χ_r^2 combined with about 95 degrees of freedom indicate that the difference between the rotation curve and each dynamical model is extremely significant, so that it could be tempting to reject any mass distribution models. However, the purpose of this discussion is not to claim that the ultimate dark matter halo of M31 has been found, but rather to put basic constraints on its parameters and to provide a summary of the dynamical content of the galaxy.

8.6.1. Mass-to-Light Ratios

We first discuss the results from SSP and HYB models. The worst results from all purely SSP models are evidence that a color-based mass-to-light of 2.2 for the bulge has to be ruled out by the present observations unless the measured rotation curve is completely uncorrect within $R = 5$ kpc, which is hard to imagine. The bulge is indeed too massive in the SSP model, as seen in the top-left graph of Figure 17.

The bulge in hybrid models still overestimates the 4 kpc dip, but the difference is not as significant as for the SSP models. Are stellar synthesis models compatible with $\Upsilon_{\text{Bulge}} = 0.8$? Reconciling them with $\Upsilon_{\text{Bulge}} = 0.8$ would require a dust-free color $B - R \sim 0.62$ mag and an intrinsic reddening $E_{B-R} \sim 1$ mag toward the direction of the M31 bulge. However, this value is 0.65 mag larger than the one adopted here. The
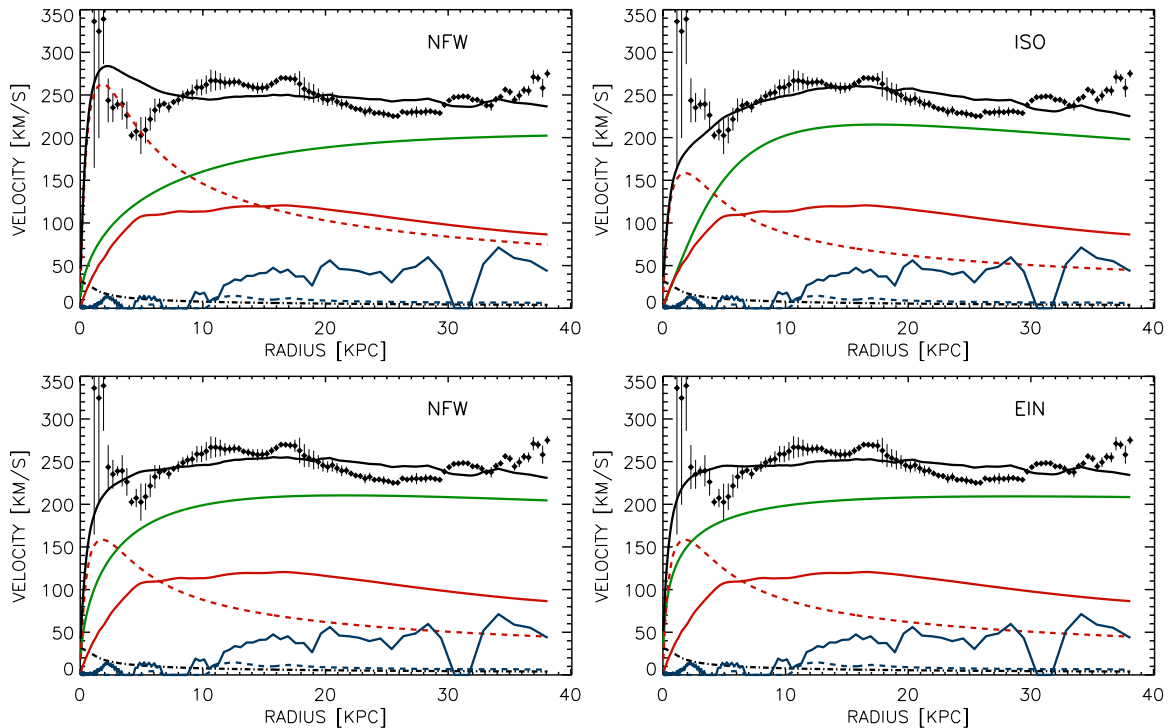
Figure 17. Mass distribution models of Messier 31. Top-left: result with bulge and disk mass-to-light ratios fixed at values $\Upsilon_{\text{Bulge}} = 2.2$ and $\Upsilon_{\text{Disk}} = 1.7$ (respectively) for a cuspy dark matter halo ("NFW"). Top-right: same as in the top-left panel but with $\Upsilon_{\text{Bulge}} = 0.8$ for a pseudo-isothermal sphere ("ISO"). Bottom: same as in the top-right panel but for the NFW cusp (left) and Einasto ("EIN," right) halos. A black dashed–dotted line is for the black hole contribution, solid and dashed blue lines for the neutral and molecular gaseous disks, solid and dashed red lines for the stellar disk and bulge, a green line for the dark matter halo and a solid black line for the overall model.

(A color version of this figure is available in the online journal.)

global reddening law for M31 has been obtained by averaging data from many line of sights and having different dust content (see, e.g., Figure 8 of Barmby et al. 2000). In view of the upper limits allowed by the uncertainties on E_{B-R} and E_{B-V} (as quoted in Barmby et al. 2000 and Williams & Hodge 2001) and of the spatial distribution of the (largest) observed reddening factors ($E_{B-V} > 0.4$ mag), which are not really concentrated in the bulge of M31 but rather in the disk dust lanes, one can hardly argue that large reddenings ($E_{B-R} > 0.7$ mag) are likely in the direction of the bulge of M31. The adopted extinction law and galaxy color thus seem realistic. Even by taking into account a lower value $\Upsilon_{\text{Bulge}} \sim 1.6$, as allowed by the uncertainties on $B - R$ and on the population synthesis models, the fit would remain of bad quality ($\chi_r^2 = 22.4$ with the pseudo-isothermal halo for instance). Note that $\Upsilon_{\text{Bulge}} \sim 1.6$ still remains at odds with the dynamical value inferred from velocity dispersion measurements. We are thus left at first sight to question about the validity of the stellar population synthesis models of Bell et al. (2003) for the bulge of M31. We do not know the implications of a fine tuning of ingredients of stellar synthesis models on the stellar evolution of a bulge with $\Upsilon_{\text{Bulge}} \sim 0.8$. A further analysis should be conducted to study this problem.

Adopting $\Upsilon_{\text{Bulge}} = 0.8$ as the most likely value implies a bulge mass-to-light ratio ~ 2.1 lower than the disk one. The stellar disk of M31 is massive but submaximum. At a radius $R = 2.15 R_d \sim 12$ kpc, which is the location of the peak velocity of an exponential disk, the ratio of the stellar disk velocity to the rotation curve is $\sim 45\%$ for $\Upsilon_{\text{Disk}} = 1.7$. Note that the ratio of the total bulge+disk velocity to the rotation curve rises to $\sim 54\%$, which still shows that the stellar component is

submaximum. Figure 17 shows that the dark matter component dominates everywhere the mass of the stellar disk, and more importantly for ΛCDM halos.

One would need $\Upsilon_{\text{Disk}} \sim 4.8$ for the galaxy to be exactly 75% of the maximum disk. This is the reason why the best-fit models correspond to the maximum disk hypothesis because they provide the largest mass-to-light ratios. There is no real consensus on the nature of disks to be maximum or submaximum since all trends are found in the observations and/or the numerical simulations (e.g., Bottema 1997; Courteau & Rix 1999; Weiner et al. 2001; Kassin et al. 2006; Zánmar Sánchez et al. 2008). A point to note here is that the population synthesis result seems not to correspond to the maximum disk solution, even though in general both assumptions are thought to be tightly linked (Bell & de Jong 2001). The upper limit of the total stellar mass implied by the BF models is $2.75 \times 10^{11}\ \mathcal{M}_\odot$. Those masses strongly differ from other stellar mass estimates of M31. Note that BF models give either unconstrained core radii or no stellar components, as seen in Table 5. The concentration and circular velocity of the NFW halo are also not consistent with expectations of similar M31-sized halos from CDM simulations (Bullock et al. 2001; Neto et al. 2007). For all these reasons, the results of BF models are rejected in the following of the analysis.

A total stellar mass of $\mathcal{M}_\star = (9.5 \pm 1.7) \times 10^{10}\ \mathcal{M}_\odot$ is derived using $\Upsilon_{\text{Disk}} = 1.7$ and $\Upsilon_{\text{Bulge}} = 0.8$ and a conservative 25% uncertainty in the disk mass-to-light ratio. The comparison with results of mass distribution modelings of M31 from other works (Kent 1989; Carignan et al. 2006; Widrow et al. 2003; Geehan et al. 2006; Tempel et al. 2007) is limited because uncorrected colors or other different photometric bands have been used for deriving the stellar mass-to-light ratios as well

as different rotation curves. An interesting result raised by Widrow et al. (2003) is that most of their numerical models point out to a higher disk mass-to-light ratio than the bulge one, which is consistent with our current analysis. However, Geehan et al. (2006) deduce a higher bulge mass-to-light ratio than for the disk (3.9 and 3.3, respectively), as well as Tempel et al. (2007). The total stellar mass compares very well with those inferred by Widrow et al. (2003), Geehan et al. (2006), or Barmby et al. (2007), but is higher than in Tempel et al. (2007, $\sim 7.5 \times 10^{10} \mathcal{M}_\odot$). Widrow et al. (2003) arrive at the conclusion that the disk mass is $< 8 \times 10^{10} \mathcal{M}_\odot$ and the bulge mass is $2.4 \times 10^{10} \mathcal{M}_\odot$, Geehan et al. (2006) report $7.2 \times 10^{10} \mathcal{M}_\odot$ for the disk and $3.2 \times 10^{10} \mathcal{M}_\odot$ for the bulge. The disk mass we deduce agrees with their results within the uncertainties while the bulge only agrees well with Widrow et al. (2003). It is worth notifying that the stellar mass quoted in Carignan et al. (2006, $2.3 \times 10^{11} \mathcal{M}_\odot$) is too high compared with all other estimates. This result is likely attributed to the too large contribution of the bulge and to the use of the best-fit/maximum disk hypothesis in our previous mass distribution model.

8.6.2. The Dark Halo of M31

The only valid hybrid models are used to discuss the basic parameters of the dark halo. We do not aim at determining an exact density shape of the dark halo of the Andromeda galaxy (core versus cusp). We only note that CDM models describe slightly better the mass distribution than the ISO model. However, this result is not really significant due to the high inferred χ^2. The parameters of the Einasto halo are in good agreement with those of empirical galaxy-sized halos modelized in numerical simulations (Merritt et al. 2006). The effective radius R_e is large and not well constrained. Actually, the Einasto model does not help to improve the quality of the fit, though it has one more free parameter than ISO or NFW models.

The concentration parameter of the NFW model is $c = 20.1 \pm 2.0$. This value is consistent with the one expected for M31-sized halos in numerical simulations ($8 < c < 20$; Bullock et al. 2001; Neto et al. 2007). It is 2.5 times lower than the one derived by Seigar et al. (2008), who used a rotation curve for the dynamical analysis as well.

8.6.3. Dynamical Content Summary

The dynamical content of M31 is calculated by averaging results from the hybrid model of the NFW halo. The total dynamical mass enclosed in the inner 38.1 kpc of M31 at the last measured data point of the H I rotation curve is $\mathcal{M}_{\mathrm{Dyn}} = (4.7 \pm 0.5) \times 10^{11} \mathcal{M}_\odot$. It represents the sum of the dark component and baryonic masses. It implies a dark-to-baryonic mass ratio of $\mathcal{M}_{\mathrm{Dark}}/\mathcal{M}_{\mathrm{Baryon}} \sim 3.7$ (79% of dark matter), and a total dynamical mass-to-light ratio $\mathcal{M}_{\mathrm{Dyn}}/L_{\mathrm{tot}} \sim 6.7$. Here, $\mathcal{M}_{\mathrm{Baryon}}$ represents the sum of the black hole, gaseous and stellar masses, $\mathcal{M}_{\mathrm{Dark}}$ the dark matter mass, and L_{tot} the total stellar luminosity in the R-band, all values integrated within $R = 38.1$ kpc. The atomic and molecular gas to stellar mass fraction is $\mathcal{M}_{\mathrm{HI+He+H_2}}/\mathcal{M}_\star = (6.2^{+1.3}_{-1.0})\%$. At the virial radius of the NFW halo ($R = 159$ kpc), the total enclosed mass of M31 is $\mathcal{M}_{\mathrm{Vir}} \sim 1.0 \times 10^{12} \mathcal{M}_\odot$.

Many works reported estimates of the total mass of M31 using different observational techniques to probe its potential. For instance, a value of $2.8 \times 10^{11} \mathcal{M}_\odot$ inside 31 kpc has been derived by Evans et al. (2000) from planetary nebulae radial velocities. Recent single-dish measurements of the rotation curve out to ~ 35 kpc led Carignan et al. (2006) to the conclusion that a total

mass of $3.4 \times 10^{11} \mathcal{M}_\odot$ was enclosed inside this radius. These values are somewhat smaller than the new mass derived inside 38.1 kpc. As for its total mass Evans et al. (2000) have used radial velocities of 15 dwarf satellites of M31 to estimate a value of $7.0^{+10.5}_{-3.5} \times 10^{11} \mathcal{M}_\odot$. Evans & Wilkinson (2000) indicate a mass of $12.3^{+18}_{-6} \times 10^{11} \mathcal{M}_\odot$ from planetary nebulae, globular clusters, and galaxy satellites radial velocity measurements inside a very large distance to the M31 nucleus (550 kpc). More recent studies of the kinematics of several substructures located in the giant stellar halo surrounding M31 help getting more information about the total mass of the galaxy. Among others, Ibata et al. (2004) measure the kinematics of stars inside the Giant Stream and model their orbits within a universal NFW profile. They deduce a total mass of $7.5^{+2.5}_{-1.3} \times 10^{11}$ inside 125 kpc, for a lower limit of $5.4 \times 10^{11} \mathcal{M}_\odot$. With more kinematical data of red giant branch (RGB) stars from the stellar halo, the same team indicates a higher virial mass $> 9 \times 10^{11} \mathcal{M}_\odot$ (Chapman et al. 2006). In the same time, numerical simulations of the merger with the Giant Stream progenitor indicate a best-fit mass of $(7.4 \pm 1.2) \times 10^{11} \mathcal{M}_\odot$ within 125 kpc (Fardal et al. 2006), very close to the result of Ibata et al. (2004). Analyses of compilations of a lot of kinematical data (rotation curves and/or velocity dispersion profiles of the M31 disk) allowed Geehan et al. (2006) to constrain a mass of $7.1 \times 10^{11} \mathcal{M}_\odot$, $10.7 \times 10^{11} \mathcal{M}_\odot$ inside 400 kpc for Tempel et al. (2007). Finally, Seigar et al. (2008) find a virial mass of $(7.3 \pm 0.2) \times 10^{11} \mathcal{M}_\odot$ for their NFW model of another composite rotation curve of M31. Our new extrapolated virial mass is thus in good agreement with the upper limits provided by Ibata et al. (2004) and Chapman et al. (2006).

9. CONCLUSION

A new deep H I mapping of Messier 31 obtained at DRAO has been presented. It combines single dish antenna and high-resolution synthesis telescope observations. The high spectral resolution of the observations show evidence that the most important contamination by the MW H I is done by a spectral component at $\sim -40 \ \mathrm{km \ s^{-1}}$. The main results from the analysis of the neutral gas distribution, kinematics, and dynamics are as follows.

1. Up to five H I peaks are detected in spectra of the M31 disk, though the detection of four or five peaks remains very rare. The majority of M31 spectra exhibit a maximum of two H I lines. The origin of all these additional lines may be internal (projection effects of gas in the warped part of the disk and in inner unresolved spiral arms, expanding clouds in star-forming regions) and/or external (extraplanar gas).

2. Ring-like and spiral-like structures are observed in the gas distribution. This is consistent with previous H I images of M31.

3. New H I structures are revealed in the outskirts of the disk. First, thin extensions (called the H I spurs) are seen to the northeast and southwest. Their size is ~ 7–10 kpc. Evidence for velocity gradients in those structures are presented. Then a faint, extended (32 kpc) and outer H I structure (called the external arm) is discovered. Contrary to every H I structures identified within the field of view, it has no morphological nor kinematical counterpart in the opposite side of the galaxy. Its peculiar kinematics can be explained by a $\sim 10°$ larger inclination and position angle than those of the disk. One of the H I spur appears as a genuine kinematical extension of that external arm.

4. A tight relationship is evidenced between the H I spurs and perturbed stellar structures (the "G1" and northeastern clumps). As possible radial outflowing motions are detected in the H I spurs, we argue that the perturbed stellar and gaseous outskirts are being torn from the M31 disk. Furthermore the external arm could be the vestige of a past tidal interaction, or even perhaps gas accretion onto the M31 disk.

5. The rotation curve is peculiar. In particular, it shows a central velocity dip at 4 kpc and a rising shape in its outer part. A peak up to 340 km s^{-1} is observed within the inner 2 kpc. Except for the inner regions, the axisymmetry of the gas rotation between the two disk halves is very good. The rotation velocity uncertainties are mostly below 10 km s^{-1}.

6. Between $R = 6$ kpc and $R = 27$ kpc a mean inclination of $74°.3 \pm 1°.1$ is derived for the H I disk of M31, for a mean position angle of $37°.7 \pm 0°.9$. A prominent H I warp is detected inside $R = 6$ kpc, where the disk appears less inclined, while another external warp detected beyond $R = 27$ kpc makes the disk being less inclined and then more inclined. The disk tilting is accompanied by a twist of the kinematical major axis.

7. The peculiar shape of the rotation curve is hardly reproduced by mass distribution models. The central velocity dip cannot be modeled by any fittings. The bulge mass-to-light ratio deduced from color-based stellar synthesis models is appropriate. A value close to the expected one from stellar velocity dispersion measurements provides better results.

8. A total stellar mass of $\mathcal{M}_\star = (9.5 \pm 1.7) \times 10^{10} \, \mathcal{M}_\odot$ is found. A dynamical enclosed mass of $\mathcal{M}_{Dyn} = (4.7 \pm 0.5) \times 10^{11} \, \mathcal{M}_\odot$ is derived at the last measured radius of the rotation curve ($R = 38$ kpc). A dark-to-baryonic mass ratio of ~4 and a total gas-to-stellar mass fraction of $(6.2^{+1.3}_{-1.0})\%$ are also derived inside that radius. The total mass of M31 extrapolated to its virial radius ($R = 159$ kpc) is $\mathcal{M}_{Vir} \sim 1.0 \times 10^{12} \, \mathcal{M}_\odot$. Both these values are consistent with those given by other works using other dynamical tracers or methods.

Several future works should be conducted with these data. A first crucial point will be to investigate the origin and evolution of the perturbed H I outskirts—the external arm and spurs. With the help of future N-body and hydrodynamical simulations, the H I kinematics should put new constraints on the mass assembly of M31. A second challenge will be to understand the origin of the peculiar velocities in the central 4 kpc. The perturbed velocities are related to the presence of the inner warp, which has perhaps been generated by an interaction with the small companion M32 (F. Combes & F. Bournaud 2009, private communication) and/or by the bar/boxy bulge perturbation. Another work will focus on a three-dimensional modeling of the datacube in order to study the origin of the gas components which are seen in addition to the warped disk of M31. Whether M31 contains the "anomalous" gas from a lagging halo, as it is observed in recent deep H I observations of other galaxies, is a question that should be addressed in such a model.

These new results obtained for M31 could only be obtained by a combination of deep exposures with high spectral resolution measurements. The quest of understanding the formation and evolution of M31 should benefit from such deep observations. We expect that future radio observatories like the Square Kilometre Array (in 2016) and its Australian and South-African precursors (in 2013) will renew the vision we have of the outer H I distribution and dynamics for millions of galaxies in the local universe. For the first time they will also allow to trace the evolution of the atomic gas as a function of redshift and thus the growth of the baryonic mass of MW- and M31-like galaxies.

REFERENCES

Bajaja, E., & Shane, W. W. 1982, A&AS, 49, 745
Barbieri, C. V., Fraternali, F., Oosterloo, T., Bertin, G., Boomsma, R., & Sancisi, R. 2005, A&A, 439, 947
Barmby, P., Huchra, J. P., Brodie, J. P., Forbes, D. A., Schroder, L. L., & Grillmair, C. J. 2000, AJ, 119, 727
Barmby, P., et al. 2006, ApJ, 650, L45
Barmby, P., et al. 2007, ApJ, 655, L61
Begeman, K. G. 1989, A&A, 223, 47
Bell, E. F., & de Jong, R. S. 2001, ApJ, 550, 212
Bell, E. F., McIntosh, D. H., Katz, N., & Weinberg, M. D. 2003, ApJS, 149, 289
Bender, R., et al. 2005, ApJ, 631, 280
Blais-Ouellette, S., Amram, P., & Carignan, C. 2001, AJ, 121, 1952
Block, D. L., et al. 2006, Nature, 443, 832
Boomsma, R., Oosterloo, T. A., Fraternali, F., van der Hulst, J. M., & Sancisi, R. 2008, A&A, 490, 555
Bottema, R. 1997, A&A, 328, 517
Braun, R. 1990, ApJS, 72, 755
Braun, R. 1991, ApJ, 372, 54
Braun, R., Thilker, D. A., Walterbos, R. A. M., & Corbelli, E. 2009, ApJ, 695, 937
Brinks, E., & Burton, W. B. 1984, A&A, 141, 195
Brinks, E., & Shane, W. W. 1984, A&AS, 55, 179
Brown, T. M., Smith, E., Guhathakurta, P., Rich, R. M., Ferguson, H. C., Renzini, A., Sweigart, A. V., & Kimble, R. A. 2006, ApJ, 636, L89
Brown, T. M., et al. 2008, ApJ, 685, L121
Bullock, J. S., Kolatt, T. S., Sigad, Y., Somerville, R. S., Kravtsov, A. V., Klypin, A. A., Primack, J. R., & Dekel, A. 2001, MNRAS, 321, 559
Capaccioli, M. 1989, in The World of Galaxies, ed. H. G. Corwin & L. Bottinelli (Berlin: Springer), 208
Cardone, V. F., Piedipalumbo, E., & Tortora, C. 2005, MNRAS, 358, 1325
Carignan, C., Chemin, L., & Foster, T. 2007, in Proc. IAU Symp. 235, Galaxy Evolution Across the Hubble Time, ed. F. Combes & J. Palous (Cambridge: Cambridge Univ. Press), 193
Carignan, C., Chemin, L., Huchtmeier, W. K., & Lockman, F. J. 2006, ApJ, 641, L109
Chapman, S. C., Ibata, R., Lewis, G. F., Ferguson, A. M. N., Irwin, M., McConnachie, A., & Tanvir, N. 2006, ApJ, 653, 255
Chapman, S. C., et al. 2008, MNRAS, 390, 1437
Chemin, L., et al. 2006, MNRAS, 366, 812
Ciardullo, R., Rubin, V. C., Ford, W. K. J., Jacoby, G. H., & Ford, H. C. 1988, AJ, 95, 438
Courteau, S., & Rix, H.-W. 1999, ApJ, 513, 561
Cram, T. R., Roberts, M. S., & Whitehurst, R. N. 1980, A&AS, 40, 215
Dame, T. M., Koper, E., Israel, F. P., & Thaddeus, P. 1993, ApJ, 418, 730
de Blok, W. J. G., Walter, F., Brinks, E., Trachternach, C., Oh, S.-H., & Kennicutt, R. C., Jr. 2008, AJ, 136, 2648
de Vaucouleurs, G. 1948, Ann. d'Astrophys., 11, 247

de Vaucouleurs, G., de Vaucouleurs, A., Corwin, H. G., Jr., Buta, R. J., Paturel, G., & Fouqué, P. 1991, Third Reference Catalog of Bright Galaxies (New York: Springer)
Dutton, A. A., Courteau, S., de Jong, R., & Carignan, C. 2005, ApJ, 619, 218
Einasto, J. 1965, Trudy Inst. Astrofiz. Alma-Ata, 5, 87
Einasto, J. 1968, Tartu Astr. Obs. Publ., 36, 414
Einasto, J. 1969, Astrofizika, 5, 137
Einasto, J., & Haud, U. 1989, A&A, 223, 89
Emerson, D. T. 1974, MNRAS, 169, 607
Evans, N. W., & Wilkinson, M. I. 2000, MNRAS, 316, 929
Evans, N. W., Wilkinson, M. I., Guhathakurta, P., Grebel, E. K., & Vogt, S. S. 2000, ApJ, 540, L9
Fardal, M. A., Babul, A., Geehan, J. J., & Guhathakurta, P. 2006, MNRAS, 366, 1012
Faria, D., Johnson, R. A., Ferguson, A. M. N., Irwin, M. J., Ibata, R., Johnston, K. V., Lewis, G. F., & Tanvir, N. 2007, AJ, 133, 1275
Ferguson, A. M. N., Irwin, M. J., Ibata, R., Lewis, G. F., & Tanvir, N. 2002, AJ, 124, 1452
Fraternali, F., & Binney, J. J. 2006, MNRAS, 366, 449
Fraternali, F., & Binney, J. J. 2008, MNRAS, 386, 935
Fraternali, F., Oosterloo, T., Sancisi, R., & van Moorsel, G. 2001, ApJ, 562, L47
Fraternali, F., van Moorsel, G., Sancisi, R., & Oosterloo, T. 2002, AJ, 123, 3124
Freeman, K. C. 1970, ApJ, 160, 811
Frenk, C. S., White, S. D. M., Davis, M., & Efstathiou, G. 1988, ApJ, 327, 507
Geehan, J. J., Fardal, M. A., Babul, A., & Guhathakurta, P. 2006, MNRAS, 366, 996
Gordon, K. D., et al. 2006, ApJ, 638, L8
Graham, A. W., & Driver, S. P. 2005, PASA, 22, 118
Graham, A. W., Merritt, D., Moore, B., Diemand, J., & Terzić, B. 2006, AJ, 132, 2701
Guhathakurta, P., et al. 2006, AJ, 131, 2497
Guibert, J. 1973, A&AS, 12, 263
Henderson, A. P. 1979, A&A, 75, 311
Higgs, L. A., & Tapping, K. F. 2000, AJ, 120, 2471
Howley, K. M., Geha, M., Guhathakurta, P., Montgomery, R. M., Laughlin, G., & Johnston, K. V. 2008, ApJ, 683, 722
Hunter, D. A., Elmegreen, B. G., & van Woerden, H. 2001, ApJ, 556, 773
Ibata, R., Chapman, S., Ferguson, A. M. N., Irwin, M., & Lewis, G. 2004, MNRAS, 351, 117
Ibata, R., Chapman, S., Ferguson, A. M. N., Lewis, G., Irwin, M., & Tanvir, N. 2005, ApJ, 634, 287
Ibata, R., Irwin, M., Lewis, G., Ferguson, A. M. N., & Tanvir, N. 2001, Nature, 412, 49
Ibata, R., Martin, N. F., Irwin, M., Chapman, S., Ferguson, A. M. N., Lewis, G., & McConnachie, A. W. 2007, ApJ, 671, 1591
Kalirai, J. S., Guhathakurta, P., Gilbert, K. M., Reitzel, D. B., Majewski, S. R., Rich, R. M., & Cooper, M. C. 2006a, ApJ, 641, 268
Kalirai, J. S., et al. 2006b, ApJ, 648, 389
Kassin, S. A., de Jong, R. S., & Weiner, B. 2006, ApJ, 643, 804
Kent, S. M. 1989, PASP, 101, 489
Klypin, A., Kravtsov, A., Valenzuela, O., & Prada, F. 1999, ApJ, 522, 82
Landecker, T. L., et al. 2000, A&AS, 145, 509
Loinard, L., Dame, T. M., Heyer, M. H., Lequeux, J., & Thaddeus, P. 1999, A&A, 351, 1087
Majewski, S. R., et al. 2007, ApJ, 670, L9

Mamon, G. A., & Łokas, E. L. 2005, MNRAS, 362, 95
Marconi, A., & Hunt, L. K. 2003, ApJ, 589, L21
Martin, N. F., Ibata, R. A., Irwin, M. J., Chapman, S., Lewis, G. F., Ferguson, A. M. N., Tanvir, N., & McConnachie, A. W. 2006, MNRAS, 371, 1983
McConnachie, A. W., Irwin, M. J., Ferguson, R. A., Ibata, R. A., Lewis, G. F., & Tanvir, N. 2005, MNRAS, 356, 979
Merritt, D., Graham, A. W., Moore, B., Diemand, J., & Terzić, B. 2006, AJ, 132, 2685
Merritt, D., Navarro, J. F., Ludlow, A., & Jenkins, A. 2005, ApJ, 624, 85
Milgrom, M. 1983, ApJ, 270, 365
Milgrom, M. 2008, arXiv:0801.3133
Navarro, J. F., Frenk, C. S., & White, S. D. M. 1996, ApJ, 462, 563
Navarro, J. F., Frenk, C. S., & White, S. D. M. 1997, ApJ, 490, 493
Neto, A. F., et al. 2007, MNRAS, 381, 1450
Newton, K., & Emerson, D. T. 1977, MNRAS, 181, 573
Nieten, C., Neininger, N., Guélin, M., Ungerechts, H., Lucas, R., Berkhuijsen, E. M., Beck, R., & Wielebinski, R. 2006, A&A, 453, 459
Oosterloo, T., Fraternali, F., & Sancisi, R. 2007, AJ, 134, 1019
Reitzel, D. B., & Guhathakurta, P. 2002, AJ, 124, 234
Richardson, J. C., et al. 2008, AJ, 135, 1998
Roberts, M. S., & Whitehurst, R. N. 1975, ApJ, 201, 327
Schlegel, D. J., Finkbeiner, D. P., & Davis, M. 1998, ApJ, 500, 525
Seigar, M. S., Barth, A. J., & Bullock, J. S. 2008, MNRAS, 389, 1911
Sérsic, J.-L. 1963, Boletin de la Asociacion Argentina de Astronomia, 6, 41
Sérsic, J.-L. 1968, Atlas de galaxias australes (Cordoba, Argentina: Observatorio Astronómico)
Spergel, D. N., et al. 2007, ApJS, 170, 377
Springel, V., et al. 2005, Nature, 435, 629
Stiehle, H., et al. 2008, in Proc. ESAC Faculty Workshop on X-Rays from Nearby Galaxies, ed. S. Carpano, M. Ehle, & W. Pietsch (Spain: ESAC), 23
Taylor, A. R., et al. 2003, AJ, 125, 3145
Tempel, E., Tamm, A., & Tenjes, P. 2007, MNRAS, submitted (arXiv: 0707.4374)
Thilker, D. A., Braun, R., Walterbos, R. A. M., Corbelli, E., Lockman, F. J., Murphy, E., & Maddalena, R. 2004, ApJ, 601, L39
Thilker, D. A., et al. 2005, ApJ, 619, L67
Unwin, S. C. 1980a, MNRAS, 190, 551
Unwin, S. C. 1980b, MNRAS, 192, 243
Unwin, S. C. 1983, MNRAS, 205, 787
van der Hulst, J. M., Terlouw, J. P., Begeman, K. G., Zwitser, W., & Roelfsema, P. R. 1992, in ASP Conf. Ser. 25, Astronomical Data Analysis, ed. D. M. Worrall, C. Biemesderfer, & J. Barnes (San Francisco, CA: ASP), 131
Verheijen, M. A. W., & Sancisi, R. 2001, A&A, 370, 765
Wakker, B. P., et al. 1999, Nature, 402, 388
Walterbos, R. A. M., & Kennicutt, R. C., Jr. 1987, A&AS, 69, 311
Walterbos, R. A. M., & Kennicutt, R. C., Jr. 1988, A&A, 198, 61
Weiner, B. J., Sellwood, J. A., & Williams, T. B. 2001, ApJ, 546, 931
Westmeier, T., Braun, R., & Thilker, D. 2005, A&A, 436, 101
Widrow, L. M., & Dubinksi, J. 2005, ApJ, 631, 838
Widrow, L. M., Perrett, K. M., & Suyu, S. H. 2003, ApJ, 588, 311
Williams, B. F., Garcia, M. R., Kong, A. K. H., Primini, F. A., King, A. R., Di Stefano, R., & Murray, S. S. 2004, ApJ, 609, 735
Williams, B. F., & Hodge, P. W. 2001, ApJ, 548, 190
Zánmar Sánchez, R., Sellwood, J. A., Weiner, B. J., & Williams, T. B. 2008, ApJ, 674, 797